

Mesh-Intrinsic GFEM: High-Order Smoothness on C^0 Unstructured Meshes

Rong Tian

Institute of Applied Physics and Computational Mathematics, Beijing 100086, China

Abstract

High-order partial differential equations (PDEs) require derivative regularity that standard C^0 finite element infrastructures do not directly provide on unstructured meshes. We propose a mesh-intrinsic generalized finite element method (MiGFEM) that reconstructs local polynomial fields on overlapping nodal patches from shared nodal unknowns and blends them by a partition of unity, without introducing extra global degrees of freedom.

The core analysis establishes a partition-of-zero (PoZ) smoothness-transfer mechanism driven by interface coherence: derivative jumps cancel exactly for polynomial reproduction and decay as $\mathcal{O}(h^{p+1-|\alpha|})$ for smooth nonpolynomial fields. On this basis, we define a PoZ-consistent intrinsic derivative that is polynomial-exact and approximation-order consistent, enabling pointwise strong-form evaluation of high-order PDEs on C^0 meshes.

For derivative-type/free boundary conditions in strong-form collocation, we introduce a boundary absorption constrained weighted least-squares strategy (BA-CWLS), which embeds boundary constraints into local patch reconstruction. This avoids globally overdetermined boundary augmentation and penalty tuning, while preserving a square sparse global system.

Numerical experiments show machine-precision patch tests, jump-decay rates consistent with theory, and robust performance on highly distorted meshes. The same mesh-intrinsic trial space supports both weak-form Galerkin and strong-form collocation discretizations, providing a unified high-order route on standard C^0 mesh infrastructures.

Keywords: Mesh-intrinsic enrichment; Partition of Zero; Strong-form discretization; Constrained weighted least-squares; Boundary-absorption

1 Introduction

Standard C^0 finite elements are not only mathematically mature but also the practical infrastructure of industrial CAE, owing to their robustness, mesh flexibility [1, 2, 3, 4, 5]. At the same time, many models of current interest—such as plate and shell bending [6, 7], strain-gradient continua [8, 9, 10, 11], phase-field formulations [12, 13, 14], and biharmonic-type systems [15]—require spatial derivatives beyond the native regularity of C^0 spaces. This creates a mismatch between standard C^0 element capabilities and the continuity requirements of high-order PDEs. From a computational perspective, strong-form discretizations are attractive in suitable regimes: if high-order PDEs can be evaluated reliably on unstructured meshes, one can reduce dependence on repeated integration by parts, high-order quadrature, and auxiliary mixed variables. The objective is to retain the C^0 FEM data structure used in industrial CAE solvers while enabling accurate and stable high-order PDE discretizations on the same infrastructure.

A broad set of high-regularity technologies has been developed to address this need. Conforming C^1 elements [16, 17, 18, 19, 20, 21, 22, 80] provide mathematically rigorous smoothness for plates and higher-order PDEs; isogeometric analysis (IGA) [23, 24, 26, 27] delivers built-in continuity through spline and

NURBS constructions; and meshfree methods [25, 28, 29, 30, 31, 32, 33, 34, 35, 36] offer strong geometric flexibility on irregular point sets. As a representative modern implementation of strong-form meshfree PDE solvers, the Medusa C++ library [73] provides a practical software reference that is directly relevant to GFDM- and RBF-FD-style workflows. More recently, Virtual Element Methods (VEM) [81, 82] and Hybrid High-Order (HHO) methods [83] have shown that high-order accuracy can be achieved on general polygonal and polyhedral meshes with standard DOF structures, albeit through different algebraic mechanisms. Together, these approaches define the current technical baseline for smooth discretization and provide key reference points for the present study.

The Manifold Method (NMM) [37, 38], the Partition of Unity Method (PUM or PUFEM) [39, 40], and the Generalized Finite Element Method (GFEM) [41, 42, 43, 44, 45] provide an appealing middle ground by decoupling local approximation quality from the global C^0 mesh topology. Developed largely in parallel—NMM in civil engineering, and PUM/GFEM in computational mathematics—they share the same structural core: a partition-of-unity blending of local approximations (“cover functions” in NMM and local enrichment functions in PUM/GFEM). Because enrichments are blended by a C^0 partition of unity, these methods preserve the sparsity and assembly infrastructure of standard FEM while enabling enhanced local approximation. In this sense, they provide a practical intermediate discretization framework between standard C^0 -FEM infrastructure and high-order discretization capability. However, traditional enrichments typically introduce node-specific degrees of freedom (DOFs), which can trigger linear dependence issues and increased computational cost [41, 42, 43, 44, 46, 47, 48, 49, 50, 51, 52, 53, 54, 55, 56, 57]. Moreover, independently constructed local enrichments often lack inter-element coherence, so high-order global smoothness is not guaranteed without additional constraints.

Building on the NMM/GFEM/PUM line, the present study develops a mesh-intrinsic formulation pathway to higher-order smoothness without adding generalized DOFs. The method follows the “extra-DOF-free” GFEM framework in [50], here termed *mesh-intrinsic enrichment*, where local approximants are reconstructed on overlapping patches from shared nodal data. The 2013 work [50] established linear independence and convergence of this formulation. Relative to that foundation, three extensions are pursued here: (i) a PoZ-based smoothness mechanism, (ii) intrinsic derivatives for pointwise strong-form evaluation on C^0 meshes, and (iii) a boundary-absorption method for primal strong forms.

We identify interface coherence as the mechanism that activates the PoZ-based smoothness transfer; the full mechanism is detailed in Section 3. In short, this leads to strict C^p continuity for polynomial-reproduction fields and asymptotic C^p continuity in the jump sense for general smooth fields, while using only standard C^0 basis functions.

The main contributions of this work are:

- A PoZ-based jump decomposition is established to make explicit the cancellation mechanism induced by interface coherence. Under polynomial reproduction, this yields strict C^p continuity; for smooth nonpolynomial fields, it gives derivative-jump decay at the approximation-consistent rate.
- Building on the same PoZ-consistent structure, a polynomial-exact intrinsic derivative is introduced. This construction enables pointwise strong-form evaluation of high-order PDEs on C^0 meshes without introducing auxiliary global DOFs.
- At the discretization level, one mesh-intrinsic trial function (locally meshfree but globally interpolatory) is formulated, allowing both weak-form Galerkin and strong-form collocation on the same C^0 mesh.
- For primal strong forms, BA-CWLS, a boundary-absorption method is proposed to enforce high-order boundary conditions (in particular traction and free-boundary conditions) exactly at the patch reconstruction level. This exact point-wise satisfaction avoids globally overdetermined boundary-

system augmentation and eliminates the need for penalty parameters, while preserving a square sparse global system.

2 Mesh-intrinsic Enrichment Formulation

2.1 Notation and Preliminaries

Consider a bounded domain $\Omega \subset \mathbb{R}^d$ equipped with a conforming finite element mesh \mathcal{T}_h and a node set $\mathcal{N} = \{x_i\}_{i \in \mathcal{N}}$. Standard C^0 finite element shape functions $\{N_i\}_{i \in \mathcal{N}}$ form a partition of unity, $\sum_{i \in \mathcal{N}} N_i(x) = 1$ for all $x \in \Omega$, and will be utilized as blending functions in the generalized framework.

Associated with each node $i \in \mathcal{N}$, we distinguish two overlapping geometric domains:

- The *support patch* $\omega_i^{\text{supp}} := \text{supp}(N_i)$, representing the region where N_i is non-vanishing. This patch governs the underlying mesh topology and baseline C^0 compatibility.
- The *nodal patch* ω_i , which is the region over which a local approximant for node i is reconstructed. Let $\mathcal{S}_i := \{j \in \mathcal{N} : x_j \in \omega_i\}$ denote the patch node set.

By construction, the nodal patch contains the support patch, $\omega_i^{\text{supp}} \subseteq \omega_i$. While ω_i^{supp} is fixed by the element geometry, the nodal patch ω_i serves as the domain for the local reconstruction operator \mathcal{R}_i , thus controlling the effective smoothness and polynomial reproduction properties of the local approximation.

The interaction between these two supports occurs at two levels. At the value level, the PoU blending restricts each reconstructed field U_i to its support ω_i^{supp} , enabling a local/compact boundary-absorption algorithm. At the derivative level, discontinuous interface contributions are canceled through the PoZ-based mechanism, whose formal definition and jump-level derivation are given in Section 3. The BA-CWLS boundary-absorption strategy (Section 6) exploits this local/compact structure to absorb boundary constraints directly into the reconstruction phase.

Throughout this work, global node indices are denoted by $i, j, k \in \mathcal{N}$. Indices ℓ, m are reserved for local indices tied to a specific patch node set \mathcal{S}_i . We adopt multi-index notation for derivatives: for $\alpha = (\alpha_1, \dots, \alpha_d) \in \mathbb{N}_0^d$, the derivative is D^α . The PoZ-related derivative identities used in the jump analysis are introduced formally in Section 3.

2.2 Method Definition

Let $\{u_i\}_{i \in \mathcal{N}}$ be the global nodal unknowns. The mesh-intrinsic GFEM is defined through a two-stage assembly process: local reconstruction followed by partition-of-unity blending.

1. Local Reconstruction. For each node $i \in \mathcal{N}$, we construct a local reconstruction operator \mathcal{R}_i that recovers the patch field $U_i(x)$ over ω_i from the common nodal unknowns $\{u_\ell\}_{\ell \in \mathcal{S}_i}$, without introducing additional local or global DOFs:

$$U_i(x) = \mathcal{R}_i(\{u_\ell\}_{\ell \in \mathcal{S}_i}), \quad x \in \omega_i. \quad (1)$$

In general, \mathcal{R}_i may be instantiated by Lagrange-type interpolation, LS/WLS polynomial reconstruction, or RBF-based reconstruction [60], as discussed in the extra-DOF-free GFEM formulation of [50]. In this work, we specifically adopt a polynomial constrained weighted least-squares (CWLS) reconstruction on each nodal patch, as detailed in Section 5.

2. PoU Blending. The global approximation $u^h(x)$ is constructed by blending these local approximants with the C^0 shape functions:

$$u^h(x) = \sum_{i \in \mathcal{N}} N_i(x) U_i(x). \quad (2)$$

Each local approximant $U_i(x)$ can be expressed as a linear combination of nodal data, $U_i(x) = \sum_{k \in \mathcal{S}_i} \Psi_k^{(i)}(x) u_k$, where $\Psi_k^{(i)}$ denotes the local reconstruction basis induced by \mathcal{R}_i . Substituting this into (2) and reordering

the summation yields:

$$u^h(x) = \sum_{k \in \mathcal{N}} \left(\sum_{i \in \mathcal{N}_k} N_i(x) \Psi_k^{(i)}(x) \right) u_k = \sum_{k \in \mathcal{N}} \phi_k(x) u_k, \quad (3)$$

where the global shape function $\phi_k(x)$ associated with node k is defined as:

$$\phi_k(x) = \sum_{i \in \mathcal{N}_k} N_i(x) \Psi_k^{(i)}(x), \quad \mathcal{N}_k := \{i \in \mathcal{N} : k \in \mathcal{S}_i\}. \quad (4)$$

This derivation shows that $u^h(x)$ is a standard nodal expansion where each global basis function ϕ_k is assembled from local contributions across all patches containing node k .

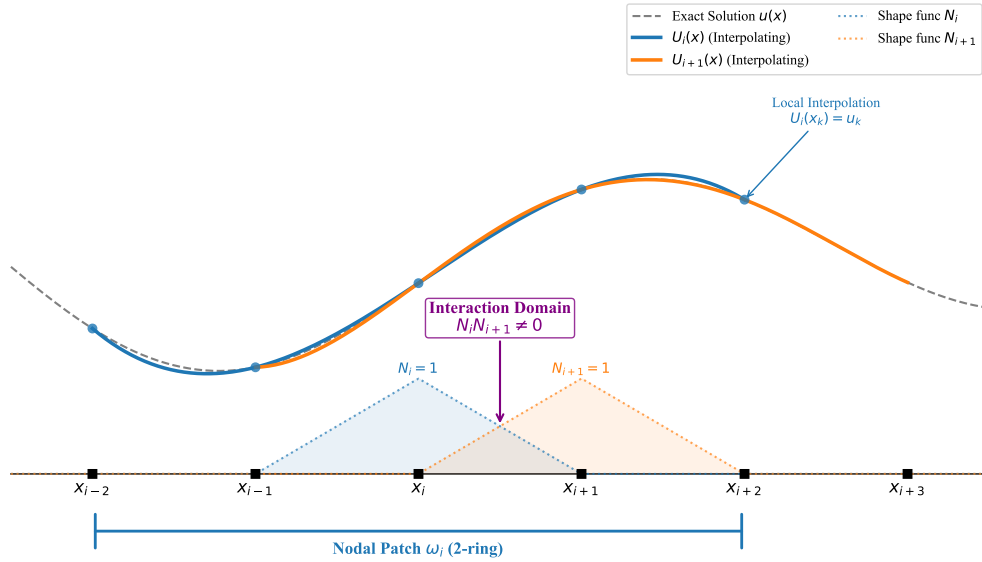


Figure 1. Illustration of the mesh-intrinsic GFEM framework in 1D: (a) Overlapping nodal patches and local reconstructions; (b) Partition of unity blending functions; (c) Resulting global approximation with enhanced continuity.

This construction, as illustrated in Fig. 1, is termed *mesh-intrinsic* because it satisfies three structural criteria that distinguish it from traditional GFEM:

1. *Shared Data Structure.* Unlike traditional GFEM which introduces node-specific enrichment DOFs, all U_i are reconstructed from the same global nodal vector $\{u_i\}$. This eliminates generalized DOFs and ill-conditioning [50, 61, 62, 63, 64, 65, 66, 67, 68].
2. *Inherent Interface Coherence.* Because neighboring nodal patches ω_i and ω_j share nodal data ($\mathcal{S}_i \cap \mathcal{S}_j \neq \emptyset$), the reconstructions U_i and U_j are coupled by design. This promotes interface coherence on overlaps; exact coherence holds for $u \in \mathcal{P}_p$ and becomes asymptotic for $u \in C^{p+1}$.
3. *Structure-Induced Smoothness.* The global regularity is not achieved by increasing the continuity of N_i (which remains C^0), but by leveraging the Partition of Zero mechanism through the aforementioned interface coherence.

Table 1 contrasts this mesh-intrinsic architecture with traditional GFEM formulations across key methodological axes.

Table 1. Comparison: Mesh-intrinsic GFEM vs. traditional GFEM

| Aspect | Traditional NMM/PUM/GFEM | Mesh-intrinsic GFEM |
|----------------------|---|--|
| Enrichment data | Node-specific function spaces \mathcal{L}_i ; independent per node | Shared global nodal vector $\{u_i\}$; mesh-intrinsic |
| Local approximants | $U_i \in \mathcal{L}_i$, constructed independently | $U_i = \mathcal{R}_i(\{u_\ell\}_{\ell \in \mathcal{S}_i})$, systematic reconstruction |
| DOF management | Generalized DOFs; linear dependence issues | Extra-DOF-free; standard FE DOFs only |
| Smoothness mechanism | None beyond C^0 PoU; enrichment incoherence preserves inter-element jumps | PoZ + interface coherence: strict C^p for \mathcal{S}_p , asymptotic C^p ($O(h^{p+1- \alpha })$ jump decay) for smooth fields |

3 Smoothness Mechanism

3.1 PoZ identity and jump-level cancellation

For a differentiable partition of unity $\{N_i\}_{i \in \mathcal{N}}$ with $\sum_{i \in \mathcal{N}} N_i(x) = 1$, differentiating with respect to a multi-index α ($|\alpha| \geq 1$) gives the derivative-space partition identity

$$\sum_{i \in \mathcal{N}} D^\alpha N_i(x) = 0, \quad |\alpha| \geq 1, \quad (5)$$

interpreted elementwise (or sidewise in trace form on interfaces) wherever the derivatives are well-defined. In what follows, this derivative-space PoU identity is referred to as PoZ for brevity.

For an internal element interface $\Gamma := \partial E^+ \cap \partial E^-$ between adjacent elements E^+ and E^- , the jump operator $[[\cdot]]_\Gamma$ is defined as $[[f]]_\Gamma := \lim_{x \rightarrow \Gamma, x \in E^+} f(x) - \lim_{x \rightarrow \Gamma, x \in E^-} f(x)$, with an arbitrary but fixed choice of interface normal orientation. For any geometric entity G (an element E or interface Γ), let $\mathcal{S}(G) := \{i \in \mathcal{N} \mid \omega_i^{\text{supp}} \cap G \neq \emptyset\}$ denote the set of indices of shape functions whose supports overlap with G .

Using the PoZ identity (5), which is elementwise and does not by itself guarantee inter-element continuity, taking the jump across an interface $\Gamma = E^+ \cap E^-$ gives

$$\sum_{i \in \mathcal{S}(\Gamma)} [[D^\alpha N_i]]_\Gamma = [[\sum_{i \in \mathcal{S}(\Gamma)} D^\alpha N_i]]_\Gamma = 0, \quad |\alpha| \geq 1. \quad (6)$$

Because $\sum_{i \in \mathcal{S}(E^\pm)} D^\alpha N_i = 0$ holds elementwise on both sides, their traces on Γ coincide, and the jump vanishes identically. This jump-level PoZ therefore cancels only the *weighted* sums of derivative jumps; it does not by itself imply global continuity without additional structural conditions (interface coherence). This jump-level PoZ is the key algebraic mechanism for the proposed smoothness enhancement.

Across an internal element interface Γ , the PoZ identity implies a simple cancellation property: for any such Γ in the finite element mesh \mathcal{T}_h and any $|\alpha| \geq 1$,

$$\sum_{i \in \mathcal{S}(\Gamma)} [[D^\alpha N_i]]_\Gamma = 0. \quad (7)$$

This follows directly from (6).

3.2 Jump decomposition and cancellation mechanism

3.2.1 Jump decomposition formula

Consider the global approximation $u^h(x) = \sum_i N_i(x)U_i(x)$, where $\{N_i\}$ is the standard C^0 PoU and $\{U_i\}$ are local approximants constructed on nodal patches ω_i via mesh-intrinsic enrichment (Section 2). For any derivative of order $|\alpha|$, the jump across an internal element interface Γ is

$$\llbracket D^\alpha u^h \rrbracket_\Gamma := \lim_{x \rightarrow \Gamma, x \in E^+} D^\alpha u^h(x) - \lim_{x \rightarrow \Gamma, x \in E^-} D^\alpha u^h(x). \quad (8)$$

Applying the multi-index Leibniz rule to $D^\alpha(N_i U_i)$ yields

$$D^\alpha u^h = \sum_i \sum_{0 \leq \beta \leq \alpha} \binom{\alpha}{\beta} (D^\beta N_i) (D^{\alpha-\beta} U_i). \quad (9)$$

Taking the jump across Γ and separating terms by the power of β gives

$$\llbracket D^\alpha u^h \rrbracket_\Gamma = \sum_{i \in \mathcal{I}(\Gamma)} \llbracket D^\alpha N_i \rrbracket_\Gamma U_i + \sum_{i \in \mathcal{I}(\Gamma)} N_i \llbracket D^\alpha U_i \rrbracket_\Gamma + \sum_{i \in \mathcal{I}(\Gamma)} \sum_{0 < \beta \leq \alpha, \beta \neq \alpha} \binom{\alpha}{\beta} \llbracket D^\beta N_i \rrbracket_\Gamma D^{\alpha-\beta} U_i. \quad (10)$$

The second term vanishes by construction: since each U_i is a single smooth function on ω_i , its traces are continuous across any element interface contained in the patch (i.e., for $\Gamma \subset \omega_i$),

$$\llbracket D^\alpha U_i \rrbracket_\Gamma = 0 \quad \text{for all } \Gamma \subset \omega_i. \quad (11)$$

Thus, the jump reduces to

$$\llbracket D^\alpha u^h \rrbracket_\Gamma = \underbrace{\sum_{i \in \mathcal{I}(\Gamma)} \llbracket D^\alpha N_i \rrbracket_\Gamma U_i}_{\text{Term I: PoZ-modulated Consistency Term}} + \underbrace{\sum_{i \in \mathcal{I}(\Gamma)} \sum_{0 < \beta \leq \alpha, \beta \neq \alpha} \binom{\alpha}{\beta} \llbracket D^\beta N_i \rrbracket_\Gamma D^{\alpha-\beta} U_i}_{\text{Term II: Cross-term Incoherence (Vanishes via Coherence)}}. \quad (12)$$

3.2.2 Interface coherence and the cancellation condition

At an internal interface Γ , we call the local reconstructions *value-coherent* if they share the same trace on Γ , i.e., $U_i(x) = U_j(x)$ for all $x \in \Gamma$ and all $i, j \in \mathcal{I}(\Gamma)$. More generally, they are *k-th order derivative coherent* if $D^\alpha U_i(x) = D^\alpha U_j(x)$ on Γ for all $|\alpha| \leq k$.

Under this coherence condition, the jump expression (12) can be factorized. Specifically, if *k-th order derivative coherence* holds on Γ , then for any $|\alpha| \leq k+1$,

$$\llbracket D^\alpha u^h \rrbracket_\Gamma = U_\Gamma \sum_{i \in \mathcal{I}(\Gamma)} \llbracket D^\alpha N_i \rrbracket_\Gamma + \sum_{0 < \beta \leq \alpha, \beta \neq \alpha} \binom{\alpha}{\beta} (D^{\alpha-\beta} U_\Gamma) \sum_{i \in \mathcal{I}(\Gamma)} \llbracket D^\beta N_i \rrbracket_\Gamma, \quad (13)$$

where U_Γ is the common interface trace induced by coherence. Since each PoZ-weighted jump sum in (13) vanishes by (7), we obtain

$$\llbracket D^\alpha u^h \rrbracket_\Gamma = 0, \quad |\alpha| \leq k+1.$$

This is the practical cancellation condition used in the subsequent smoothness analysis.

3.3 Interface coherence and patch consistency

3.3.1 Patch consistency as a sufficient condition

In the present setting, we refer to *exact patch consistency* when two local reconstructions coincide throughout their overlap region:

$$U_i(x) = U_j(x) \quad \text{for all } x \in \omega_i \cap \omega_j. \quad (14)$$

This condition is sufficient (though not necessary) for interface coherence. Indeed, if $\Gamma \subset \omega_i \cap \omega_j$, then exact overlap agreement implies identical traces on Γ ; if U_i and U_j are C^k on their patches, their derivatives up to order k also coincide on Γ . In other words, exact patch consistency on overlaps directly yields k -th order derivative coherence on the corresponding internal element interfaces.

3.3.2 Structural enforcement of patch consistency

The mesh-intrinsic enrichment framework (Section 2) promotes this patch consistency by design through three structural mechanisms:

1. **Shared nodal data.** All local approximants $\{U_i\}$ are reconstructed from the same global nodal vector $\{u_i\}_{i \in \mathcal{N}}$, coupling overlaps through common data.
2. **Compatible reconstruction.** Neighboring patches employ the same reconstruction operator and polynomial completeness order p .
3. **Overlapping topology.** The condition $\mathcal{S}_i \cap \mathcal{S}_j \neq \emptyset$ guarantees that reconstructions on $\omega_i \cap \omega_j$ are coupled.

When the target field is a polynomial $u \in \mathcal{P}_p$, these mechanisms ensure that U_i and U_j both reproduce u exactly on the overlap, yielding *exact patch consistency*. For general smooth solutions $u \in C^{p+1}(\Omega)$, exact patch consistency does not hold, but the mechanism yields *asymptotic patch consistency*; correspondingly, the jump decay follows Eq. (17), where the discrepancy $(U_i - U_j)$ decays at the rate of the local reconstruction error. This structural patch consistency activates the PoZ, providing a symmetric pathway to high-order smoothness without the need for C^1 basis functions.

3.4 Strict C^p -continuity for polynomial fields

For polynomial target fields $u \in \mathcal{P}_p$, if each local reconstruction is polynomially consistent of degree p , then exact patch consistency is achieved, i.e., $U_i(x) = u(x)$ on each ω_i . Consequently, neighboring patches are derivative-coherent up to order p on their overlaps and on the internal element interfaces $\Gamma = \partial E^+ \cap \partial E^-$ contained in those overlaps.

Substituting this interface coherence into the jump decomposition and using the PoZ cancellation gives, for any internal interface Γ and any multi-index α with $|\alpha| \leq p$,

$$[[D^\alpha u^h]]_\Gamma = 0. \quad (15)$$

In computational terms, this means MiGFEM passes polynomial patch tests exactly up to degree p , and inter-element derivative jumps up to order p vanish in exact arithmetic. The corresponding numerical evidence is reported in Section 8.

3.5 Asymptotic C^p -continuity for smooth fields

For smooth nonpolynomial fields, continuity is expected in an asymptotic sense rather than exactly at finite mesh size. The analysis below uses two standard ingredients: (i) nodal-patch reconstruction errors satisfy

$$\|D^\mu(U_i - u)\|_{L^\infty(\omega_i)} \leq C_e h^{p+1-|\mu|}, \quad |\mu| \leq p,$$

under the usual MLS approximation assumptions [58, 59]; and (ii) PoU derivatives satisfy $\|D^\beta N_i\| = \mathcal{O}(h^{-|\beta|})$ with bounded overlap multiplicity [4, 5].

To make the cancellation mechanism explicit, write the smooth field locally as $u = T_p + r$, where T_p is the degree- p Taylor polynomial (the leading term) and $r = \mathcal{O}(h^{p+1})$ is the remainder. Define the local reconstruction error by $e_i := U_i - u$. Substituting $U_i = u + e_i$ into the jump decomposition (12), the contributions

associated with the common leading polynomial part T_p cancel exactly through PoZ, and we obtain

$$\llbracket D^\alpha u^h \rrbracket_\Gamma = \sum_{i \in \mathcal{I}(\Gamma)} \sum_{0 < \beta \leq \alpha} \binom{\alpha}{\beta} \llbracket D^\beta N_i \rrbracket_\Gamma D^{\alpha-\beta} e_i, \quad |\alpha| \leq p. \quad (16)$$

Therefore, inter-element jumps are controlled solely by reconstruction errors.

For each term in (16), we first use the product estimate in L^∞ :

$$\|\llbracket D^\beta N_i \rrbracket_\Gamma D^{\alpha-\beta} e_i\|_{L^\infty(\Gamma)} \leq \|\llbracket D^\beta N_i \rrbracket_\Gamma\|_{L^\infty(\Gamma)} \|D^{\alpha-\beta} e_i\|_{L^\infty(\omega_i)}.$$

Then, using the PoU scaling and local reconstruction bound,

$$\|\llbracket D^\beta N_i \rrbracket_\Gamma\|_{L^\infty(\Gamma)} \leq C_N h^{-|\beta|}, \quad \|D^{\alpha-\beta} e_i\|_{L^\infty(\omega_i)} \leq C_e h^{p+1-|\alpha-\beta|},$$

so

$$\|\llbracket D^\beta N_i \rrbracket_\Gamma D^{\alpha-\beta} e_i\|_{L^\infty(\Gamma)} \leq C_N C_e h^{p+1-|\alpha|}.$$

Substituting this bound into (16), and using that both the number of active indices $i \in \mathcal{I}(\Gamma)$ and the number of multi-indices $\beta \leq \alpha$ are finite and h -independent (with bounded overlap multiplicity), we obtain

$$\|\llbracket D^\alpha u^h \rrbracket_\Gamma\|_{L^\infty(\Gamma)} \leq \widehat{C} h^{p+1-|\alpha|}, \quad |\alpha| \leq p, \quad (17)$$

with \widehat{C} independent of h .

Hence, for $u \in C^{p+1}(\Omega)$, the mesh-intrinsic approximation is asymptotically C^p -continuous in the jump sense:

$$\llbracket D^\alpha u^h \rrbracket_\Gamma = \mathcal{O}(h^{p+1-|\alpha|}), \quad |\alpha| \leq p.$$

This is a mesh-refinement statement and does not imply classical global C^p regularity at finite h . Numerical verification is reported in Section 8.

4 PoZ-Consistent Intrinsic Derivative

4.1 Definition from PoZ decomposition

Consider the global approximation

$$u^h(x) = \sum_{i \in \mathcal{N}} N_i(x) U_i(x). \quad (18)$$

Its Leibniz derivative is decomposed as

$$D^\alpha u^h(x) = \underbrace{\sum_{i \in \mathcal{N}} N_i(x) D^\alpha U_i(x)}_{\widetilde{D}^\alpha u^h(x)} + \underbrace{\sum_{i \in \mathcal{N}} \sum_{0 < \beta \leq \alpha} \binom{\alpha}{\beta} D^\beta N_i(x) D^{\alpha-\beta} U_i(x)}_{R^\alpha(x)}. \quad (19)$$

Hence we define the intrinsic derivative and remainder by

$$\widetilde{D}^\alpha u^h := \sum_{i \in \mathcal{N}} N_i D^\alpha U_i, \quad (20)$$

$$D^\alpha u^h - \widetilde{D}^\alpha u^h =: R^\alpha. \quad (21)$$

4.2 PoZ cancellation mechanism

Using the PoZ identity from Section 3, the mixed term R^α is handled directly:

- For $u \in \mathcal{P}_p$ (exact patch consistency / interface coherence),

$$R^\alpha = \sum_{0 < \beta \leq \alpha} \binom{\alpha}{\beta} \left(\sum_{i \in \mathcal{N}} D^\beta N_i \right) D^{\alpha-\beta} P \equiv 0, \quad (22)$$

so

$$\tilde{D}^\alpha u^h = D^\alpha u^h \quad (|\alpha| \leq p). \quad (23)$$

- For $u \in C^{p+1}(\Omega)$ (asymptotic patch consistency / interface coherence), the same cancellation removes the polynomial-leading part in the local Taylor expansion; the residual follows the scaling established in Section 3:

$$R^\alpha = \mathcal{O}\left(h^{p+1-|\alpha|}\right). \quad (24)$$

Therefore, the estimate is not merely a bound on derivatives of blending functions; it is an estimate directly for

$$R^\alpha = D^\alpha u^h - \tilde{D}^\alpha u^h.$$

Hence, replacing the full Leibniz derivative by the intrinsic derivative discards only a higher-order remainder and does not introduce additional order loss beyond patch-reconstruction accuracy.

Therefore intrinsic differentiation is the PoZ-consistent preferred differentiation rule: exact for polynomial fields and high-order consistent for smooth fields.

4.3 Consistency and continuity properties

The intrinsic derivative has three practical properties used later in discretization design:

1. (*Polynomial exactness.*) If $u \in \mathcal{P}_p$, then $\tilde{D}^\alpha u^h = D^\alpha u^h$ for $|\alpha| \leq p$.
2. (*Approximation-order consistency.*) For $u \in C^{p+1}(\Omega)$,

$$\|D^\alpha u - \tilde{D}^\alpha u^h\|_{L^\infty(\Omega)} \leq Ch^{p+1-|\alpha|}. \quad (25)$$

Hence replacing $D^\alpha u^h$ by $\tilde{D}^\alpha u^h$ does not introduce additional order loss beyond patch-reconstruction accuracy.

3. (*Inter-element continuity behavior.*) For polynomial fields, jumps vanish as in Eq. (15). For general smooth fields, the classical derivative is only asymptotically smooth with jump decay Eq. (17), while $\tilde{D}^\alpha u^h$ is globally continuous as a C^0 -PoU-weighted combination of smooth local functions.

4.4 Implication for weak-form stress/strain evaluation

In weak-form Galerkin use, $\tilde{D}^\alpha u^h$ gives a built-in *smooth* derivative field for stress/strain evaluation. It is polynomial-exact and consistency-preserving, so high-order post-processing can be performed directly from reconstruction without separate recovery operators.

4.5 Implication for strong-form discretizations

For high-order strong forms, pointwise residual evaluation requires bounded derivatives. Using classical Leibniz differentiation of a globally C^0 PoU blend introduces interface-distribution contributions in mixed terms. The intrinsic derivative avoids this by differentiating only smooth local reconstructions:

$$\tilde{\Delta} u^h := \sum_{i \in \mathcal{N}} N_i \Delta U_i, \quad \tilde{\Delta}^2 u^h := \sum_{i \in \mathcal{N}} N_i \Delta^2 U_i. \quad (26)$$

These are pointwise computable and continuous, enabling strong-form collocation on C^0 meshes without requiring C^1/C^2 inter-element continuity of N_i [4, 5].

5 Local reconstruction operator and Kronecker delta properties

This section presents the patch-reconstruction procedure and its resulting algebraic properties in the global system. We use constrained weighted least-squares (CWLS) to build polynomial patch reconstructions with explicit nodal interpolation constraints. While other reconstruction backends (e.g., RBF-based reconstruction; Section 7.5) are also compatible with the framework, CWLS is adopted here as a robust and practical implementation for engineering computations.

5.1 Patch definition

For each node $i \in \mathcal{N}$ (referred to herein as the *patch star node*, in the NMM spirit of a star-centered local cover/patch description [37, 38]), a nodal patch ω_i is constructed by aggregating elements within s topological layers around the node. The associated sampling set $\mathcal{S}_i \subset \mathcal{N}$ consists of all nodes contained in ω_i . To ensure the local problem is well-posed for a polynomial of degree p , the layer depth s is selected such that $|\mathcal{S}_i| \geq \dim \mathcal{P}_p$. On the unstructured triangular meshes used in this work, $s = p/2 + 1$ is used for interior nodes (Fig. 2a), and the patch at a boundary node is extended inwards to secure sufficient sampling size (Fig. 2b). This strategy ensures nearly the same sampling-set size for all nodes.

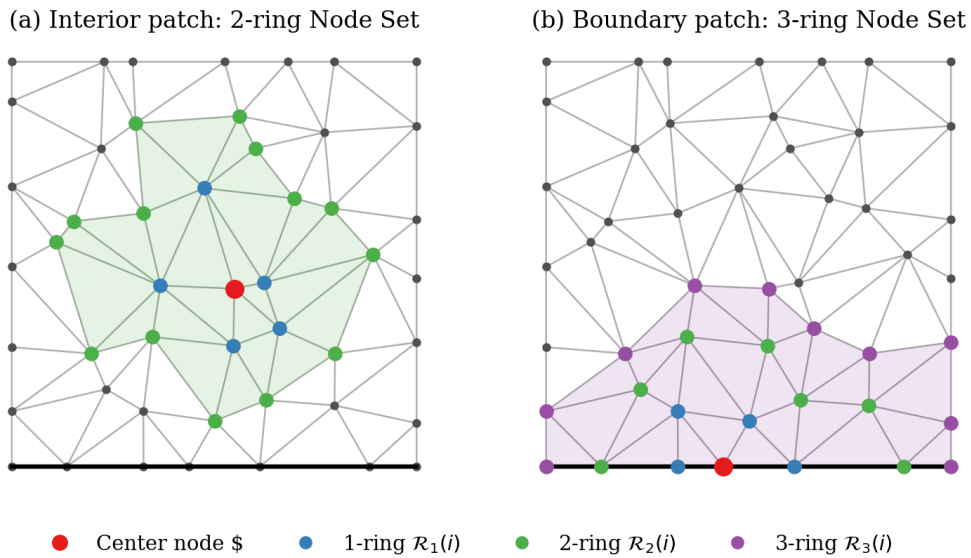


Figure 2. Patch node sets and stencils on an unstructured triangular mesh. (a) Interior patch with $s = 2$ layers. (b) Boundary patch with $s = 3$ layers.

5.2 Constrained weighted least-squares (CWLS) formulation

The local approximant $U_i(x)$ on patch ω_i is sought as a polynomial expansion in scaled local coordinates $\xi = (x - x_i)/\rho_i$, where ρ_i is a characteristic patch radius. We write

$$U_i(x) = p(\xi)^\top a_i, \quad \xi = \frac{x - x_i}{\rho_i}, \quad (27)$$

where $p(\xi)$ is the basis vector for \mathcal{P}_p and a_i is the coefficient vector.

The coefficient vector a_i is determined by minimizing a weighted discrete L^2 error over the sampling set \mathcal{S}_i , subject to an exact interpolation constraint at the patch star node x_i :

$$\min_{a \in \mathbb{R}^{\mathcal{Q}}} \frac{1}{2} \|\mathbf{W}_i(\mathbf{P}_i a - u_{\mathcal{S}_i})\|_2^2 \quad \text{s.t.} \quad c_i^\top a = u_i, \quad (28)$$

where \mathbf{P}_i is the Vandermonde-like sampling matrix with rows $p((x_k - x_i)/\rho_i)^\top$ for $k \in \mathcal{S}_i$, \mathbf{W}_i is a diagonal weight matrix, and $c_i = p(0)$ corresponds to the evaluation at the patch star node.

Using Lagrange multipliers, define

$$\mathbf{A}_i := \mathbf{P}_i^\top \mathbf{W}_i^2 \mathbf{P}_i, \quad \mathbf{C}_i := c_i^\top, \quad b_i := u_i.$$

Then the standard CWLS KKT system is [78, 79]

$$\begin{bmatrix} \mathbf{A}_i & \mathbf{C}_i^\top \\ \mathbf{C}_i & 0 \end{bmatrix} \begin{bmatrix} a_i \\ \lambda_i \end{bmatrix} = \begin{bmatrix} \mathbf{P}_i^\top \mathbf{W}_i^2 u_{\mathcal{S}_i} \\ b_i \end{bmatrix}. \quad (29)$$

This is exactly the base form reused in BA-CWLS (Section 6), where \mathbf{C}_i is augmented by supplementary constraint rows.

The coefficient map is written explicitly as

$$\mathbf{M}_i = \begin{bmatrix} \mathbf{I}_{\mathcal{Q}} & \mathbf{0} \end{bmatrix} \begin{bmatrix} \mathbf{A}_i & \mathbf{C}_i^\top \\ \mathbf{C}_i & 0 \end{bmatrix}^{-1} \begin{bmatrix} \mathbf{P}_i^\top \mathbf{W}_i^2 \\ \mathbf{E}_i \end{bmatrix}, \quad (30)$$

where $\mathbf{I}_{\mathcal{Q}} \in \mathbb{R}^{\mathcal{Q} \times \mathcal{Q}}$ is the identity matrix and $\mathbf{E}_i \in \mathbb{R}^{1 \times |\mathcal{S}_i|}$ is the row selector such that $\mathbf{E}_i u_{\mathcal{S}_i} = u_i$. Hence

$$a_i = \mathbf{M}_i u_{\mathcal{S}_i}, \quad (31)$$

with $\mathbf{M}_i \in \mathbb{R}^{\mathcal{Q} \times |\mathcal{S}_i|}$ precomputed from local geometry, basis, and weights.

Substituting (31) back into (27) gives the explicit form of the local approximant:

$$U_i(x) = p(\xi)^\top \mathbf{M}_i u_{\mathcal{S}_i} = \sum_{k \in \mathcal{S}_i} \Psi_k^{(i)}(x) u_k. \quad (32)$$

5.3 Kronecker delta property and derivative evaluation

Kronecker delta property. A direct consequence of the patch star interpolation constraint ($U_i(x_i) = u_i$) is that the global mesh-intrinsic approximation preserves the Kronecker delta property of the underlying finite element mesh [1, 2, 3]. Evaluating the global field $u^h(x) = \sum_i N_i(x) U_i(x)$ at any node x_j , and noting that $N_i(x_j) = \delta_{ij}$, we obtain:

$$u^h(x_j) = \sum_{i \in \mathcal{N}} N_i(x_j) U_i(x_j) = U_j(x_j) = u_j. \quad (33)$$

This property simplifies the imposition of essential boundary conditions, as nodal values on the boundary directly correspond to physical field values. In the strong-form collocation variants we therefore impose Dirichlet data by row replacement at boundary collocation points; in weak-form Galerkin we instead enforce Dirichlet conditions weakly (e.g., Nitsche) to preserve consistency with the nonvanishing boundary traces of ϕ_k [4, 69].

Efficient derivative evaluation. The polynomial structure of U_i allows for efficient derivative evaluation. Since U_i is a polynomial in scaled coordinates, its derivatives are obtained analytically from the basis derivatives:

$$D^\alpha U_i(x) = \rho_i^{-|\alpha|} (D_\xi^\alpha p(\xi))^\top \mathbf{M}_i u_{\mathcal{S}_i}. \quad (34)$$

This expression involves only precomputed matrices and basis evaluations, avoiding numerical differentiation during the assembly process. The mapping matrices \mathbf{M}_i are computed once during pre-processing, making the evaluation of high-order spatial derivatives (e.g., Δ^2) computationally efficient.

6 Boundary Absorption-CWLS (BA-CWLS)

The CWLS formulation of Section 5.2 imposes a single interpolation constraint at the patch star node x_i . This section generalizes the construction by augmenting the constraint block with an arbitrary set of linear pointwise constraints, while keeping the same weighted least-squares objective (28) and the same normal-equation kernel $\mathbf{A}_i = \mathbf{P}_i^\top \mathbf{W}_i^2 \mathbf{P}_i$. We refer to the resulting formulation as Boundary Absorption-CWLS (BA-CWLS), abbreviated as BA below.

The key observation is that any linear constraint expressible in row form with respect to the polynomial coefficient vector a_i can be appended directly to the CWLS KKT system (29). Because the reconstruction is local, constraint effects propagate to the global system exclusively through the reconstruction mapping—no additional global equations, penalty parameters, or Lagrange multiplier fields are introduced. Consequently, BA-CWLS is applicable wherever boundary or interface conditions can be expressed as pointwise linear constraints on the local polynomial coefficients. This covers, in particular, strong-form collocation with derivative-type boundary conditions and pointwise essential constraints in weak-form settings; it does not, however, replace integral-form boundary treatments such as Nitsche’s method.

6.1 Augmented constraint block

Recall that the base CWLS constraint is defined by $\mathbf{C}_i := c_i^\top \in \mathbb{R}^{1 \times Q}$ and $b_i := u_i$ (Section 5.2). Suppose that, in addition, a set of n_i supplementary linear pointwise constraints is imposed on patch i :

$$r_{i,k}^\top a_i = g_{i,k}, \quad k = 1, \dots, n_i, \quad (35)$$

where each $r_{i,k} \in \mathbb{R}^Q$ is a constraint row vector determined by the type and location of the constraint, and $g_{i,k}$ is the prescribed data. Collecting these rows into

$$\mathbf{R}_i := \begin{bmatrix} r_{i,1}^\top \\ \vdots \\ r_{i,n_i}^\top \end{bmatrix} \in \mathbb{R}^{n_i \times Q}, \quad \mathbf{g}_i := \begin{bmatrix} g_{i,1} \\ \vdots \\ g_{i,n_i} \end{bmatrix} \in \mathbb{R}^{n_i}, \quad (36)$$

the BA-CWLS formulation is obtained from (28) by augmenting only the constraint block:

$$\min_{a_i \in \mathbb{R}^Q} \frac{1}{2} \|\mathbf{W}_i(\mathbf{P}_i a_i - u_{\mathcal{I}_i})\|_2^2 \quad \text{s.t.} \quad \underbrace{c_i^\top a_i = u_i}_{\text{base CWLS}}, \quad \underbrace{\mathbf{R}_i a_i = \mathbf{g}_i}_{\text{absorbed constraints}}. \quad (37)$$

The objective and the base constraint are identical to (28); the only addition is the second constraint group.

6.2 KKT system: augmentation of (29)

Define the augmented constraint matrix and right-hand side by stacking the base CWLS constraint $\mathbf{C}_i = c_i^\top$ with the supplementary rows \mathbf{R}_i :

$$\bar{\mathbf{C}}_i := \begin{bmatrix} \mathbf{C}_i \\ \mathbf{R}_i \end{bmatrix} = \begin{bmatrix} c_i^\top \\ \mathbf{R}_i \end{bmatrix} \in \mathbb{R}^{(1+n_i) \times Q}, \quad \bar{b}_i := \begin{bmatrix} b_i \\ \mathbf{g}_i \end{bmatrix} = \begin{bmatrix} u_i \\ \mathbf{g}_i \end{bmatrix} \in \mathbb{R}^{1+n_i}. \quad (38)$$

Replacing $\mathbf{C}_i \rightarrow \bar{\mathbf{C}}_i$ and $b_i \rightarrow \bar{b}_i$ in the CWLS KKT system (29) gives the BA-CWLS KKT system:

$$\begin{bmatrix} \mathbf{A}_i & \bar{\mathbf{C}}_i^\top \\ \bar{\mathbf{C}}_i & \mathbf{0} \end{bmatrix} \begin{bmatrix} a_i \\ \lambda_i \end{bmatrix} = \begin{bmatrix} \mathbf{P}_i^\top \mathbf{W}_i^2 u_{\mathcal{I}_i} \\ \bar{b}_i \end{bmatrix}, \quad \mathbf{A}_i = \mathbf{P}_i^\top \mathbf{W}_i^2 \mathbf{P}_i. \quad (39)$$

The normal-equation block \mathbf{A}_i and the right-hand-side data block $\mathbf{P}_i^\top \mathbf{W}_i^2 u_{\mathcal{S}_i}$ are unchanged from (29); only the constraint block is enlarged. For $n_i = 0$, Eq. (39) reduces identically to (29).

6.3 Coefficient map: generalization of (30)

Let $\mathbf{E}_i \in \mathbb{R}^{1 \times |\mathcal{S}_i|}$ be the row selector such that $\mathbf{E}_i u_{\mathcal{S}_i} = u_i$ (same as in (30)). Partition the constraint right-hand side \bar{b}_i into the nodal-data component (driven by $u_{\mathcal{S}_i}$) and the prescribed-data component (driven by g_i) via

$$\mathbf{T}_i^{(u)} := \begin{bmatrix} \mathbf{E}_i \\ \mathbf{0} \end{bmatrix} \in \mathbb{R}^{(1+n_i) \times |\mathcal{S}_i|}, \quad \mathbf{T}_i^{(g)} := \begin{bmatrix} \mathbf{0} \\ \mathbf{I}_{n_i} \end{bmatrix} \in \mathbb{R}^{(1+n_i) \times n_i}, \quad (40)$$

so that $\bar{b}_i = \mathbf{T}_i^{(u)} u_{\mathcal{S}_i} + \mathbf{T}_i^{(g)} g_i$. The coefficient vector then decomposes as

$$a_i = \mathbf{M}_i^{(u)} u_{\mathcal{S}_i} + \mathbf{M}_i^{(g)} g_i, \quad (41)$$

where $\mathbf{M}_i^{(u)} \in \mathbb{R}^{Q \times |\mathcal{S}_i|}$ and $\mathbf{M}_i^{(g)} \in \mathbb{R}^{Q \times n_i}$ are obtained by the same extraction pattern as (30), with $\mathbf{C}_i \rightarrow \bar{\mathbf{C}}_i$:

$$\mathbf{M}_i^{(u)} = [\mathbf{I}_Q \quad \mathbf{0}] \begin{bmatrix} \mathbf{A}_i & \bar{\mathbf{C}}_i^\top \\ \bar{\mathbf{C}}_i & \mathbf{0} \end{bmatrix}^{-1} \begin{bmatrix} \mathbf{P}_i^\top \mathbf{W}_i^2 \\ \mathbf{T}_i^{(u)} \end{bmatrix}, \quad (42)$$

$$\mathbf{M}_i^{(g)} = [\mathbf{I}_Q \quad \mathbf{0}] \begin{bmatrix} \mathbf{A}_i & \bar{\mathbf{C}}_i^\top \\ \bar{\mathbf{C}}_i & \mathbf{0} \end{bmatrix}^{-1} \begin{bmatrix} \mathbf{0} \\ \mathbf{T}_i^{(g)} \end{bmatrix}. \quad (43)$$

For $n_i = 0$, $\bar{\mathbf{C}}_i = \mathbf{C}_i$, $\mathbf{T}_i^{(u)} = \mathbf{E}_i$, and $\mathbf{M}_i^{(g)}$ vanishes; Eq. (42) then reduces to the base CWLS coefficient map (30), i.e. $\mathbf{M}_i^{(u)} = \mathbf{M}_i$.

6.4 Local approximant: generalization of (32)

Substituting (41) into the polynomial expansion (27) gives

$$U_i(x) = \underbrace{p(\xi)^\top \mathbf{M}_i^{(u)} u_{\mathcal{S}_i}}_{=\sum_{j \in \mathcal{S}_i} \Psi_j^{(i)}(x) u_j} + \underbrace{p(\xi)^\top \mathbf{M}_i^{(g)} g_i}_{=\sum_{k=1}^{n_i} \Phi_{i,k}(x) g_{i,k}}. \quad (44)$$

The first term is the DOF-driven (homogeneous) part, retaining exactly the same local shape functions $\Psi_j^{(i)}$ and polynomial-reproducing properties as CWLS (32). The second term is the data-driven (particular) part, encapsulating the absorbed constraint data. For interior patches ($n_i = 0$), the second term vanishes and (44) coincides with (32).

6.5 Global assembly: right-hand-side absorption

Let \mathcal{L} denote an arbitrary linear differential operator. Applying \mathcal{L} to the global approximation $u^h = \sum_i N_i U_i$ at an evaluation point x_c (which may be a collocation node, a quadrature point, or a subdomain centre, depending on the discretization) and using the split (44) yields

$$\sum_j w_{c_j}^{(u)} u_j = f(x_c) - \sum_{i: x_c \in \omega_i^{\text{supp}}} \sum_{k=1}^{n_i} w_{c_{ik}}^{(g)} g_{i,k}, \quad (45)$$

where $w_{c_j}^{(u)}$ and $w_{c_{ik}}^{(g)}$ are stencil weights induced by applying \mathcal{L} to $\Psi_j^{(i)}$ and $\Phi_{i,k}$, respectively. Thus the constraint data enter solely through the right-hand side; the global system matrix structure and dimension are unchanged, and no additional global equation rows are introduced. For weak-form Galerkin the same algebra applies: the data-driven part contributes to the load vector through the variational residual, leaving the stiffness matrix unaltered.

6.6 Admissibility conditions

To ensure that the augmented KKT system (39) remains well-posed:

1. *Constraint compatibility.* The total number of constraints must not exceed the polynomial dimension: $1 + n_i \leq Q$.
2. *Constraint independence.* The augmented constraint matrix $\bar{\mathbf{C}}_i$ must have full row rank.
3. *Polynomial consistency preservation.* The supplementary constraints must be consistent with the polynomial reproduction properties of CWLS: for any $u \in \mathcal{P}_p$, the exact polynomial coefficients must satisfy the constraint equations. This condition is automatically met when the constraint rows $r_{i,k}$ are derived from differential operators or point-evaluation functionals applied to $p(\xi)$.

Condition 3 is the fundamental prerequisite for the intrinsic derivative mechanism: if boundary absorption were to destroy the p -th order exactness of the local reconstruction, the resulting intrinsic derivatives would lose their high-order consistency. The diagnostics for verifying these conditions in practice—constraint load ratio, polynomial patch-test residuals, and post-solve constraint satisfaction error—are reported in the numerical examples.

6.7 Boundary Absorption for Traction and Free Boundaries

In strong-form collocation, derivative-type boundary conditions (traction, free-surface, or flux conditions) must be enforced explicitly. A straightforward approach—appending global boundary-equation rows at each boundary collocation point—leads to a heavily overdetermined system, degrading algebraic conditioning and solver efficiency. The BA-CWLS construction established above offers a local alternative: boundary constraints are directly absorbed into the patch reconstruction phase, so that the global system retains its square, sparse structure.

6.7.1 Active boundary trace and pointwise sampling

For a point $x \in \Gamma_N$, the MiGFEM approximation reads

$$u^h(x) = \sum_{i \in \mathcal{I}(x)} N_i(x) U_i(x), \quad \mathcal{I}(x) := \{i \in \mathcal{N}_h : x \in \omega_i^{\text{supp}}\}. \quad (46)$$

Using the intrinsic derivative, the pointwise boundary condition $\tilde{\mathcal{B}}u^h(x) = \bar{g}(x)$ becomes

$$\tilde{\mathcal{B}}u^h(x) = \sum_{i \in \mathcal{I}(x)} N_i(x) \mathcal{B}U_i(x). \quad (47)$$

Due to the partition of unity $\sum N_i(x) = 1$, satisfying the local constraint $\mathcal{B}U_i(x) = \bar{g}(x)$ on every participating patch guarantees exact satisfaction of the global boundary condition, *without explicit cross-patch coupling equations or penalty parameters*.

The boundary absorption is imposed on every patch whose PoU support intersects Γ_N . We define the active boundary trace for patch i as

$$\Gamma_i^N := \omega_i^{\text{supp}} \cap \Gamma_N, \quad (48)$$

and the finite set of boundary sampling points within each patch as

$$X_i^N := \{x_{i,1}, \dots, x_{i,n_i}\} \subset \Gamma_i^N. \quad (49)$$

To circumvent the ill-posedness of normal vectors at geometric singularities (corners, etc.), the boundary sampling points are restricted to the interiors of boundary edges, explicitly excluding mesh nodes.

6.7.2 Scalar boundary flux (Laplacian/biharmonic)

For a scalar boundary flux condition $\partial u / \partial n = \bar{g}$, the constraint row at boundary point x_b is

$$r_i(x_b) := \rho_i^{-1} \left(n_x(x_b) \frac{\partial p}{\partial \xi} \Big|_{\xi_b} + n_y(x_b) \frac{\partial p}{\partial \eta} \Big|_{\xi_b} \right), \quad \xi_b = (x_b - x_i) / \rho_i, \quad (50)$$

which is directly substituted into the BA-CWLS supplementary constraint matrix \mathbf{R}_i defined in (36).

6.7.3 Traction boundary (linear elasticity)

For linear elasticity, let the local vector polynomial coefficients be $a_i = [a_i^{(x)}; a_i^{(y)}] \in \mathbb{R}^{2Q}$. At each boundary point $x_{i,k} \in X_i^N$, the Cauchy traction condition induces two scalar constraint rows:

$$r_i^{(t_x)}(x_{i,k}), \quad r_i^{(t_y)}(x_{i,k}),$$

for the two traction components. The pointwise traction constraints are therefore

$$r_i^{(t_x)}(x_{i,k}) a_i = \bar{t}_x(x_{i,k}), \quad r_i^{(t_y)}(x_{i,k}) a_i = \bar{t}_y(x_{i,k}), \quad k = 1, \dots, n_i. \quad (51)$$

Each sampled boundary point contributes two scalar constraints in two dimensions, both embedded into the BA-CWLS framework (37).

6.7.4 Effect on the global system

By the coefficient decomposition (41), the absorbed boundary data enter the global system exclusively through right-hand-side corrections via (45). The global system matrix remains square and sparse; boundary data influence the strong-form solution via the local reconstructions active at each collocation point. For internal patches with $\Gamma_i^N = \emptyset$ (i.e., $n_i = 0$), the BA-CWLS system reduces identically to standard CWLS.

7 Unified Discretizations for Strong and Weak Forms

A distinguishing feature of the mesh-intrinsic framework is that it provides a single approximation structure capable of supporting both weak-form (variational) and strong-form (collocation) solution. Unlike traditional methods where C^0 elements are restricted to weak forms of second-order problems, the proposed method allows for a unified treatment. This section derives both discretizations from a common weighted-residual statement, demonstrating that a single trial space accommodates both integration-by-parts formulations and pointwise collocation.

7.1 Unified Trial Space

The global approximation is given by the expansion:

$$u^h(x) = \sum_{k \in \mathcal{N}} \phi_k(x) u_k. \quad (52)$$

The basis functions ϕ_k (defined in Eq. (4)) are globally C^0 but possess high-order intrinsic smoothness on patches. This dual nature allows them to be operated on by either:

1. The **Leibniz derivative** D^α (distributional), suitable for weak forms with integration by parts.
2. The **Intrinsic derivative** \tilde{D}^α (pointwise), suitable for strong forms without integration by parts.

7.2 Weighted-Residual Formulation

Consider the linear boundary value problem:

$$\mathcal{L}u = f \quad \text{in } \Omega, \quad (53)$$

$$\mathcal{B}_D u = g \quad \text{on } \partial\Omega_D, \quad (54)$$

$$\mathcal{B}_N u = h \quad \text{on } \partial\Omega_N. \quad (55)$$

A consistent weighted-residual statement is: Find u^h such that for all test functions w :

$$\int_{\Omega} w (\mathcal{L}u^h - f) d\Omega + \int_{\partial\Omega_D} \eta \bar{w} (\mathcal{B}_D u^h - g) ds + \int_{\partial\Omega_N} \bar{\bar{w}} (\mathcal{B}_N u^h - h) ds = 0. \quad (56)$$

From this starting point, two distinct discretization paths emerge.

7.3 Weak-Form Galerkin Formulation with Leibniz Derivatives

The weak form is obtained by applying integration by parts to the domain term $\int_{\Omega} w \mathcal{L} u^h$. Using the Green's identity $\int w \mathcal{L} u = a(w, u) - \int_{\partial\Omega} w \mathcal{T}(u)$, we reduce the derivative order on the trial function.

- **Derivative evaluation:** The bilinear form $a(\cdot, \cdot)$ employs the standard Leibniz derivatives $D^\alpha u^h$. Since integration by parts lowers the required continuity, the C^0 nature of u^h is sufficient for second-order problems (e.g., Laplace), while fourth- and higher-order problems require additional treatment.
- **Boundary Conditions:** Since the basis functions ϕ_k do not vanish on $\partial\Omega_D$ (being constructed from overlapping patches), Dirichlet conditions are enforced weakly via Nitsche's method to preserve symmetry and consistency.

The resulting discrete system $K\mathbf{u} = \mathbf{F}$ is symmetric and positive-definite for elliptic problems, resembling a standard high-order FEM system.

7.4 Strong-Form Collocation Formulation with Intrinsic Derivatives

The strong-form branch is obtained by enforcing the governing differential equation directly at collocation entities, i.e., without integration by parts. Let $\{\xi_m\}_{m=1}^{M_\Omega} \subset \Omega$ denote interior collocation points, $\{\xi_m^D\}_{m=1}^{M_D} \subset \partial\Omega_D$ Dirichlet points, and $\{\xi_m^N\}_{m=1}^{M_N} \subset \partial\Omega_N$ derivative/free-boundary points. The interior residual equations read

$$\mathcal{L} u^h(\xi_m) = f(\xi_m), \quad m = 1, \dots, M_\Omega, \quad (57)$$

where the derivatives in $\mathcal{L} u^h$ are evaluated by the intrinsic derivative (Section 4). The intrinsic derivative is computed as

$$\tilde{D}^\alpha u^h(x) := \sum_{k \in \mathcal{N}} N_k(x) D^\alpha U_k(x), \quad (58)$$

which is used in all strong-form evaluations in place of direct Leibniz differentiation of the global $u^h = \sum_k N_k U_k$. This preserves the intended polynomial consistency of the local reconstruction in strong-form collocation.

Boundary equations are imposed by a split strategy consistent with the primal nodal unknown structure (e.g., two sets of essential boundary conditions per node in biharmonic problems):

- **Dirichlet boundary:** strong imposition by row replacement/elimination at $\partial\Omega_D$ collocation points.
- **Derivative/free boundary:** local BA-CWLS absorption (Section 6), so derivative constraints are incorporated at patch level rather than appended as an additional global overdetermined block.

Within this framework, three collocation layouts are considered.

1. **Nodal collocation (MiGFEM-NC):** $\mathcal{L} u^h(\xi_k) = f(\xi_k)$ at interior nodes; the resulting algebraic system is naturally square.
2. **Cell collocation (MiGFEM-CC):** $\mathcal{L} u^h(\xi_m) = f(\xi_m)$ at element points (typically centroids or quadrature points); the system is in general rectangular and solved in a least-squares sense when overdetermined.
3. **Subdomain collocation (MiGFEM-SD):** $\int_{\Omega_c} (\mathcal{L} u^h - f) d\Omega = 0$ on node-centered control subdomains Ω_c ; the assembled system is naturally square.

Hence, NC/CC/SD are not different approximation spaces; they are three algebraic realizations of the same mesh-intrinsic trial space, distinguished only by test layout (pointwise vs. subdomain averaging) and the resulting linear-system structure.

7.5 Comparisons of MiGFEM-NC with GFDM and RBF-FD Stencil Formulations

At interior node x_i , the Kronecker property $N_k(x_i) = \delta_{ik}$ reduces the intrinsic strong-form evaluation to $\mathcal{L}u^h(x_i) = \mathcal{L}U_i(x_i)$. Since $U_i(x) = \sum_{j \in \mathcal{S}_i} \Psi_j^{(i)}(x)u_j$, this gives the canonical nodal stencil equation

$$\sum_{j \in \mathcal{S}_i} w_{ij}u_j = f(x_i), \quad w_{ij} := [\mathcal{L}\Psi_j^{(i)}(x)]_{x=x_i}, \quad (59)$$

which has the same algebraic stencil form as generalized finite difference methods (GFDM) [70, 71, 72, 74] and RBF-FD methods [75, 76, 77]. The distinction is the weight-construction backend: GFDM uses polynomial moment fitting, RBF-FD uses PHS-RBF interpolation with polynomial augmentation, and MiGFEM-NC uses CWLS patch reconstruction embedded in a global PoU field.

MiGFEM-NC is therefore not only a nodal stencil method. It also retains an explicit global trial field $u^h(x) = \sum_k N_k(x)U_k(x)$ and a pointwise intrinsic derivative $\tilde{D}^\alpha u^h(x) = \sum_k N_k(x)D^\alpha U_k(x)$ evaluable at arbitrary points. In addition, PoZ identities $\sum_k D^\beta N_k = 0$ preserve polynomial consistency between nodal-stencil reduction and full Leibniz differentiation, while supplying the global jump-decay mechanism established in Section 3. These global structures are not implied by isolated nodal stencils alone.

7.6 Unified Perspective and Discretization Paths

The unification is structural: one mesh-intrinsic trial space and one weighted-residual starting point support both weak-form Galerkin and strong-form collocation.

The distinction lies in the derivative evaluation and the treatment of boundary conditions. Weak-form discretization employs Leibniz derivatives together with integration by parts, whereas strong-form discretization relies on PoZ-consistent intrinsic derivatives. In the strong-form setting, constraints are enforced via the BA-CWLS strategy introduced in Section 6; however, this strategy is not inherently tied to a single discretization path.

Accordingly, WG is square/symmetric; NC and SD are naturally square; CC is generally overdetermined and solved in least squares. Table 2 summarizes these differences.

Table 2. Comparison of discretization paths.

| Feature | Weak Form (Galerkin) | Strong Form (Collocation) |
|--------------------------|--|--|
| Trial space | Same C^0 mesh-intrinsic basis | |
| Degrees of freedom | Standard FE nodal DOFs (no extra DOFs) | |
| Stress/strain evaluation | Intrinsic derivatives; no extra recovery | |
| Derivative Evaluation | Leibniz D^α (Distributional) | Intrinsic \tilde{D}^α (Pointwise) |
| Integration by Parts | Yes (Reduces order) | No (Primal high-order) |
| Continuity Req. | C^0 (for 2nd order) | PoZ-induced Smoothness |
| Linear System | Square, Symmetric | Square or Overdetermined |

8 Numerical Verification

This section provides a staged numerical verification of the proposed Mesh-Intrinsic GFEM (MiGFEM). The objectives are twofold: (i) to validate PoZ-induced smoothness transfer in the approximation space, and (ii) to evaluate strong- and weak-form discretizations constructed on the same mesh-intrinsic trial space.

To separate approximation-space behavior from PDE-solver effects, the tests are organized from low-coupling diagnostics to full discretizations. The sequence is: PoZ smoothness diagnostics, high-order patch

tests, second-order elasticity benchmarks, fourth-order biharmonic benchmarks, and conditioning/robustness studies.

8.1 Implementation overview and algorithmic setting

8.1.1 Local approximation space

The local CWLS reconstruction and PoU blending follow Sections 2 and 5. Here we report only the default benchmark parameters. Table 3 lists the reference settings for polynomial degree p , layer depth s , weight kernel, and patch scaling radius ρ_i . Unless otherwise stated, meshes are conforming triangulations generated by uniform refinement; optional random perturbations of interior nodes (with amplitudes specified per test) are introduced to assess distortion robustness.

Table 3. Reference CWLS reconstruction parameters used across numerical tests (unless otherwise specified).

| Parameter | Default choice |
|--------------------------|---|
| Polynomial degree | p (varies by test, typically $p = 3-6$) |
| Layer depth | $s = p/2 + 1$ interior, $s + 1$ boundary (unless noted) |
| Stencil size requirement | $ \mathcal{S}_i \geq \dim \mathcal{P}_p$ |
| Weight kernel | fixed-order power kernel (power = 3 unless noted) |
| Scaling radius | ρ_i chosen as local patch radius |

8.1.2 Discretization schemes

We evaluate four discretization schemes on the same CWLS-based trial space:

- **Strong-form collocation (NC, CC, SD):** We test the three variants defined in Section 7.4—Nodal Collocation (NC), Cell Collocation (CC), and Subdomain Collocation (SD). NC and SD produce square systems, whereas CC collocates at element points and is solved as an overdetermined least-squares problem. All three variants use polynomial-exact intrinsic derivatives for pointwise PDE evaluation.
- **Weak-form Galerkin (WG):** We include a standard variational formulation as the weak-form reference, with Dirichlet boundary conditions imposed weakly via Nitsche’s method.

This design isolates approximation-space effects from the choice of test/discretization strategy.

8.1.3 Integration and error metrics

Numerical integration for weak-form (WG) and subdomain (SD) terms uses standard Dunavant rules on triangles, with algebraic precision matched to the polynomial degree of the integrand.

For asymptotic smoothness analysis, inter-element continuity is measured by

$$J_m := \max_{\Gamma \in \mathcal{E}_{\text{int}}} \left\| \llbracket \partial_n^m u^h \rrbracket \right\|_{L^\infty(\Gamma)}, \quad m = 1, 2, \dots, 5, \quad (60)$$

where \mathcal{E}_{int} is the set of internal interfaces. In implementation, J_m is computed as the maximum pointwise jump over all internal edges and edge Gauss points.

Two derivative-evaluation modes are used:

- **Intrinsic derivatives (NC, CC, SD):** $\partial^\alpha u^h$ is evaluated using the intrinsic derivative.

- **Leibniz/direct derivatives (WG):** derivatives are evaluated by the standard Leibniz rule on element interiors.

Since intrinsic differentiation does not introduce additional order reduction, strong- and weak-form results on the same benchmark can be cross-checked for consistency. Accordingly, jump metrics are used to quantify inter-element smoothness, while normed errors quantify solution accuracy.

For scale-independent reporting, we also use the normalized jump metric

$$\widehat{J}_m := \frac{J_m}{\max_{\Gamma,q} |\partial_n^m u^h(\xi_q)|},$$

with the denominator evaluated on internal-edge quadrature points using the same derivative definition as in J_m .

For displacement-based elasticity tests, we report standard relative errors in L^2 , H^1 , and stress-based energy norms. For fourth-order biharmonic tests, we report element-integrated relative L_h^2 and H_h^2 errors (defined in the corresponding biharmonic subsection).

8.2 Mechanism Verification: PoZ Smoothness-Transfer Diagnostics

This subsection verifies PoZ smoothness transfer in the approximation space, independent of PDE discretization details. The focus is to test whether shared-data CWLS reconstructions and PoU blending produce the interface coherence predicted by the theory.

We consider two complementary diagnostics:

- **Case 1 (strict test):** polynomial reproduction, where exact C^p continuity is expected in exact arithmetic;
- **Case 2 (rate test):** smooth non-polynomial data, where asymptotic jump decay is expected under mesh refinement.

The smooth benchmark field used in Case 2 is

$$\mathbf{u}(x,y) = \begin{pmatrix} \cos(y) \sin(x) \\ \cos(x) \sin(y) \end{pmatrix}, \quad (x,y) \in [-1,1]^2. \quad (61)$$

Unless stated otherwise, derivative jumps are measured by the pointwise interface metric in Eq. (60), i.e., the maximum over all internal edges and edge Gauss points.

8.2.1 Case 1: Polynomial reproduction (exact C^p -continuity)

Objective. To verify that exact polynomial reproduction by local CWLS reconstructions implies exact inter-element derivative coherence (up to order p) in exact arithmetic.

Setup. On triangular meshes of $[-1,1]^2$, we prescribe

$$u(x,y) = (1+x+y)^5,$$

and use degree- $p = 5$ CWLS reconstruction on each patch with nodal values sampled from the exact polynomial. Since \mathcal{P}_5 is contained in the reconstruction space, local approximants are polynomially exact in exact arithmetic.

Results. The measured intrinsic-derivative jumps remain at roundoff level, consistent with the exact C^p prediction. Over meshes from 11×11 to 41×41 , J_0 stays in $\mathcal{O}(10^{-13} \sim 10^{-11})$, while J_4 remains small (up to $\mathcal{O}(10^{-7})$ on the finest mesh). The increase with derivative order is consistent with floating-point amplification in high-order differentiation rather than a violation of the theoretical exact-continuity result. Representative values are listed in Table 4.

Table 4. Case 1: Jump metrics for polynomial solution $u(x,y) = (1+x+y)^5$ with $p = 5$.

| Mesh | h | J_0 | J_1 | J_2 | J_3 | J_4 |
|----------------|--------|------------------------|------------------------|------------------------|------------------------|-----------------------|
| 11×11 | 0.2000 | 3.21×10^{-13} | 1.58×10^{-11} | 2.51×10^{-11} | 1.19×10^{-10} | 1.01×10^{-9} |
| 21×21 | 0.1000 | 1.37×10^{-12} | 2.79×10^{-11} | 7.55×10^{-11} | 9.56×10^{-10} | 1.41×10^{-8} |
| 41×41 | 0.0500 | 1.32×10^{-11} | 4.80×10^{-11} | 2.49×10^{-10} | 8.67×10^{-9} | 2.58×10^{-7} |

8.2.2 Case 2: Asymptotic C^p -continuity under mesh refinement

Objective. To test the PoZ-predicted asymptotic decay of interface derivative jumps for smooth non-polynomial fields.

Setup. The trigonometric field in Eq. (61) is interpolated on uniformly refined triangular meshes (11×11 , 21×21 , 41×41 , 81×81) with zero node perturbation. For $p = 3, 4, 5$, CWLS uses

$$s = \max\{2, \lfloor (p+1)/2 \rfloor\},$$

with a fixed power-kernel weight (power 3). We compute J_m for $m = 1, 2, 3$ and fit slopes from $\log J_m$ versus $\log h$, then compare against the predicted rates $p+1-m$.

Results. For $|\alpha| = m \leq p$, theory gives

$$[[D^\alpha u^h]]_\Gamma = \mathcal{O}(h^{p+1-|\alpha|}),$$

in agreement with Eq. (17). Observed slopes closely follow this trend: for $p = 3$, $(J_1, J_2, J_3) = (2.80, 1.87, 0.85)$ vs. $(3, 2, 1)$; for $p = 4$, $(3.99, 2.98, 2.07)$ vs. $(4, 3, 2)$; for $p = 5$, $(4.89, 3.92, 2.89)$ vs. $(5, 4, 3)$. Figure 3 reports the corresponding convergence curves.

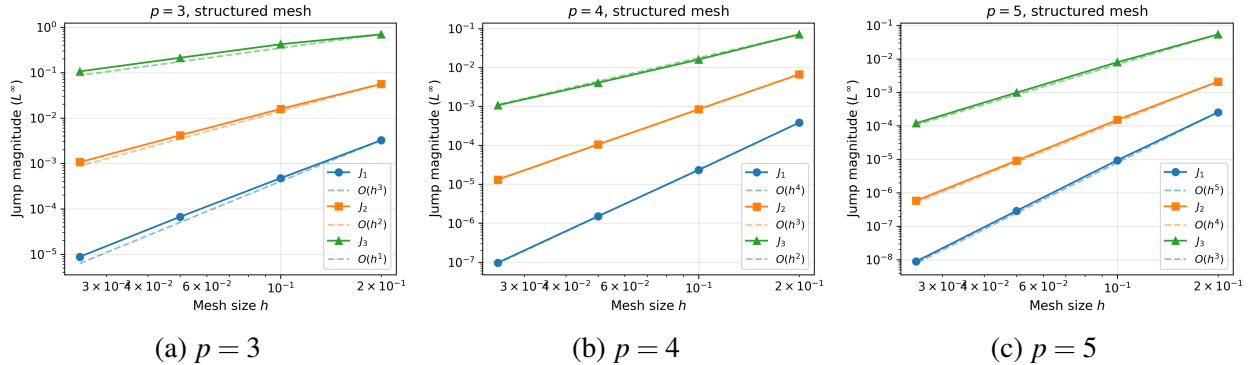


Figure 3. Case 2: Asymptotic C^p -continuity on triangular meshes with zero node perturbation for $p = 3, 4, 5$. The plots show the decay of pointwise L^∞ jump metrics J_m under uniform h -refinement, with dashed reference lines indicating the predicted rates $\mathcal{O}(h^{p+1-m})$.

8.3 High-Order Patch Tests

This subsection checks polynomial consistency at the PDE level. Unlike the smoothness diagnostics in Section 8, these tests verify whether the assembled strong/weak formulations reproduce manufactured polynomial solutions at near-roundoff accuracy when the CWLS space is polynomially complete.

8.3.1 Second-order PDEs: Elasticity patch tests

Objective. To verify exact polynomial reproduction for second-order elasticity across the MiGFEM discretization variants, and to confirm that the observed accuracy is limited primarily by floating-point, conditioning, and boundary-enforcement effects.

Setup. We consider plane stress on $\Omega = (0, 5)^2$ with the manufactured polynomial field

$$\mathbf{u}(x, y) = \begin{pmatrix} (10 + x + y)^p \\ (10 + x + y)^p \end{pmatrix}, \quad (62)$$

from which \mathbf{b} , ε , and σ are derived analytically. Uniformly refined triangular meshes are used. Boundary displacement data on $\partial\Omega$ are imposed either (i) by direct DOF elimination using the Kronecker property $\phi_j(x_k) = \delta_{jk}$ (with exact boundary-traction functional retained in WG for variational consistency), or (ii) by symmetric Nitsche enforcement with $\beta = \mathcal{O}(E/h)$.

Results. Table 5 reports errors for NC, CC, SD, and WG. The strong-form variants (NC/CC/SD) attain near-roundoff displacement accuracy ($\mathcal{O}(10^{-10})$) and very small high-order derivative errors (about $\mathcal{O}(10^{-8})$ in fourth derivatives), consistent with exact polynomial consistency up to numerical effects. WG with symmetric Nitsche yields errors around $\mathcal{O}(10^{-7})$, consistent with weak boundary-penalty approximation; WG with direct elimination gives comparable levels when the exact boundary traction functional is included.

Table 5. Elasticity patch test on triangular CWLS space (11×11 , $p = 4$, $s = 3$): errors for displacement and derivatives up to fourth order relative to the exact solution.

| Method | $\ e_u\ _\infty$ | $\ e_{D^1 u}\ _\infty$ | $\ e_{D^2 u}\ _\infty$ | $\ e_{D^3 u}\ _\infty$ | $\ e_{D^4 u}\ _\infty$ |
|-------------------------|------------------------|------------------------|------------------------|------------------------|------------------------|
| NC | 4.07×10^{-10} | 6.22×10^{-10} | 1.20×10^{-9} | 9.60×10^{-9} | 2.24×10^{-8} |
| CC | 1.26×10^{-9} | 8.88×10^{-10} | 3.99×10^{-9} | 2.61×10^{-8} | 6.66×10^{-8} |
| SD | 1.28×10^{-9} | 6.38×10^{-10} | 5.09×10^{-9} | 5.08×10^{-8} | 1.27×10^{-7} |
| WG (Nitsche) | 2.29×10^{-7} | 1.60×10^{-7} | 2.19×10^{-7} | 8.71×10^{-7} | 1.68×10^{-6} |
| WG (direct elimination) | 2.30×10^{-7} | 1.66×10^{-7} | 2.53×10^{-7} | 7.03×10^{-7} | 1.84×10^{-6} |

Remark (Boundary enforcement in WG). Strong-form collocation enforces essential boundary conditions directly at nodes, preserving the polynomial consistency of the interior reconstruction. In contrast, the WG formulation, derived from integration by parts, includes boundary traction terms. While standard FEM shape functions vanish on the boundary under direct elimination, MiGFEM basis functions can be nonzero on boundary edges that do not contain node k because PoU blending couples overlapping patches. Consequently, exact consistency in the WG patch test requires either the inclusion of the exact boundary traction functional (as done here) or a consistent weak enforcement such as Nitsche’s method; otherwise, residual boundary terms dominate the polynomial test even when the interior reconstruction is exact.

8.3.2 Fourth-order PDEs: Biharmonic patch tests

Objective. To verify polynomial consistency of the strong-form MiGFEM discretization of the biharmonic problem, i.e., exact reproduction at the algebraic level up to roundoff and conditioning effects.

Setup. We solve a clamped-plate benchmark $\Delta^2 u = f$ on $\Omega = (0, 1)^2$ using an exact polynomial solution with degree $p \geq 4$. The CWLS local space is chosen to reproduce this polynomial exactly, and clamped boundary conditions $(u, \partial_n u)$ are prescribed on $\partial\Omega$.

Results. Table 6 shows near-roundoff displacement errors for NC and CC ($\mathcal{O}(10^{-13})$), with fourth-derivative errors around $\mathcal{O}(10^{-8})$. SD remains highly accurate but exhibits larger fourth-derivative errors (about $\mathcal{O}(10^{-6})$), consistent with stronger sensitivity to quadrature and local conditioning in the evaluation of fourth-order residuals. Overall, the patch test indicates that MiGFEM with intrinsic derivatives yields a consistent discretization of the biharmonic problem on standard C^0 triangulations, without resorting to globally C^1 -conforming elements, although classical pointwise evaluation of the biharmonic operator generally requires regularity beyond C^1 .

Table 6. Biharmonic patch test on triangular CWLS space (11×11 , $p = 5$, $s = 3$): displacement and derivative errors (up to fourth order).

| Method | $\ e_u\ _{L^2}$ | $\ e_{D^1 u}\ _\infty$ | $\ e_{D^2 u}\ _\infty$ | $\ e_{D^3 u}\ _\infty$ | $\ e_{D^4 u}\ _\infty$ |
|--------|------------------------|------------------------|------------------------|------------------------|------------------------|
| NC | 2.08×10^{-13} | 4.95×10^{-12} | 4.43×10^{-11} | 1.37×10^{-9} | 2.05×10^{-8} |
| CC | 2.14×10^{-13} | 5.63×10^{-12} | 5.30×10^{-11} | 1.84×10^{-9} | 2.52×10^{-8} |
| SD | 5.87×10^{-12} | 9.37×10^{-11} | 1.49×10^{-9} | 4.65×10^{-8} | 1.13×10^{-6} |

8.4 Performance on Second-Order PDEs: Elasticity Benchmarks

This subsection evaluates the second-order elasticity performance of MiGFEM from four complementary viewpoints: (i) strong/weak formulation consistency under mixed boundary conditions, (ii) DOF-normalized comparison against standard p -FEM and PUFEM, (iii) conditioning scaling under refinement, and (iv) robustness under mesh perturbation.

8.4.1 Strong/weak form comparison under mixed Dirichlet–Neumann boundaries

Objective. To compare strong- and weak-form MiGFEM behavior on the same mixed-boundary benchmark, and to test whether BA-based Neumann treatment preserves the accuracy of QR-based overdetermined enforcement while keeping the global system square.

Setup. We consider the manufactured plane-stress problem on $\Omega = (0, 5)^2$ with

$$\mathbf{u}(x, y) = \begin{pmatrix} \cos(y) \sin(x) \\ \cos(x) \sin(y) \end{pmatrix}, \quad (63)$$

from which body force and boundary traction are obtained analytically. Mixed boundary data are prescribed: displacement on $\partial\Omega_D$ and traction on $\partial\Omega_N$.

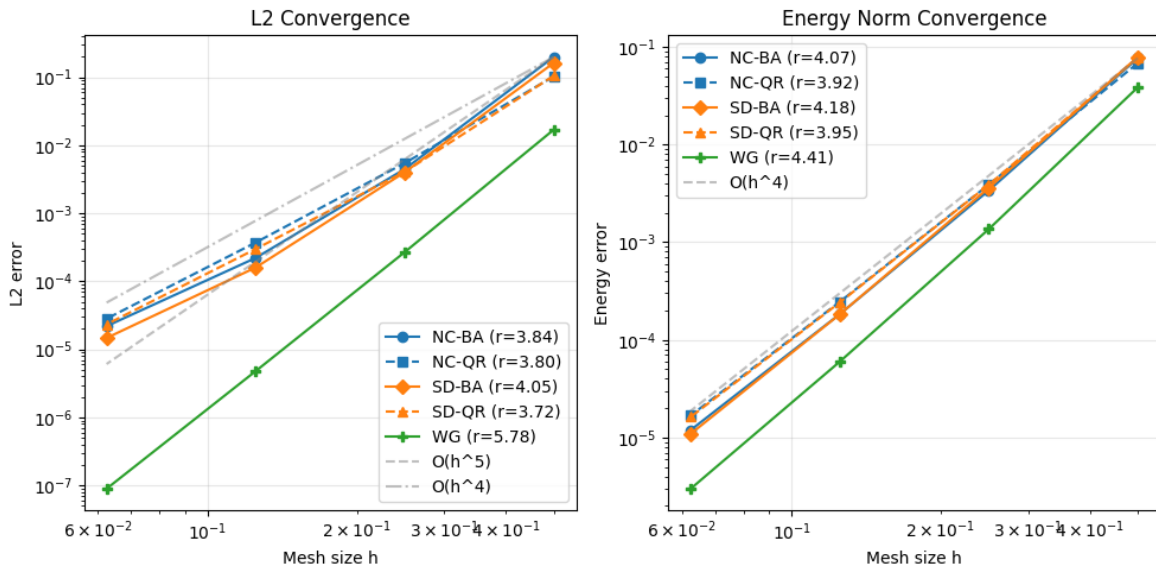
All variants use the same MiGFEM trial space and are tested for $p = 4$ and $p = 6$:

- **NC-QR:** nodal collocation with strong Dirichlet enforcement and QR-based overdetermined Neumann enforcement;
- **NC-BA:** nodal collocation with strong Dirichlet enforcement and local BA absorption of Neumann boundaries;
- **SD-QR:** subdomain collocation with strong Dirichlet enforcement and QR-based overdetermined Neumann enforcement;
- **SD-BA:** subdomain collocation with strong Dirichlet enforcement and local BA absorption of Neumann boundaries;
- **WG:** weak-form reference with symmetric Nitsche Dirichlet enforcement and natural Neumann treatment.

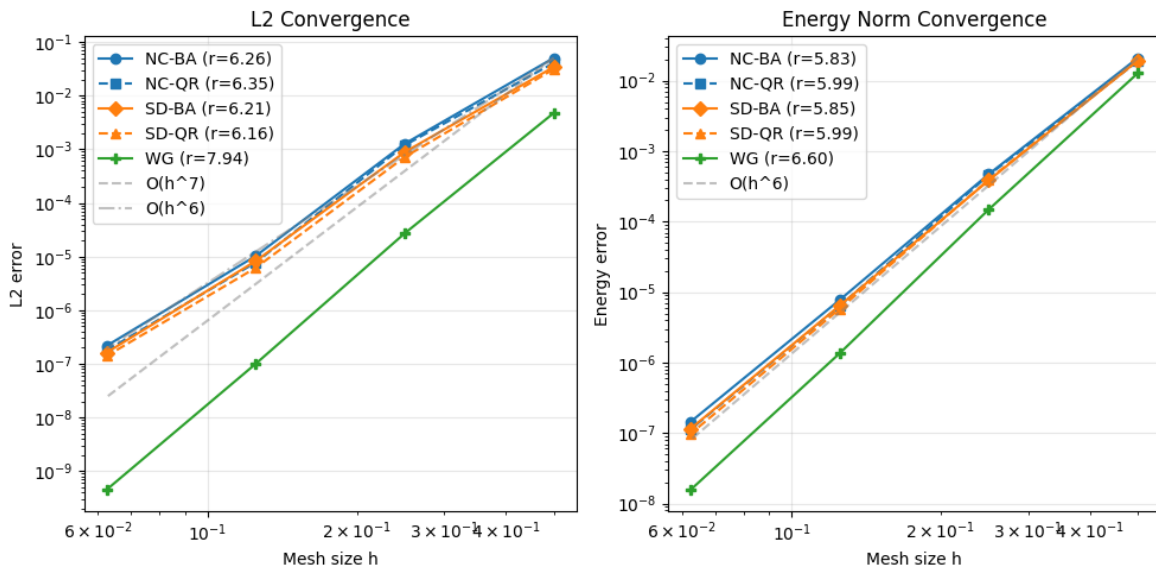
We report displacement L^2 error, stress-based energy error, and total wall-clock time on the mesh sequence 11×11 – 81×81 .

Results. Figure 4 and Table 7 show that WG follows the expected weak-form optimal trend. For both $p = 4$ and $p = 6$, the strong-form NC/SD variants exhibit the same rate pattern under BA and QR boundary treatments: the energy-norm convergence remains near optimal, whereas the displacement L^2 convergence shows a reproducible one-order reduction. Quantitatively, for $p = 4$, L^2 rates are 3.7–4.0 and energy rates are 3.9–4.2; for $p = 6$, L^2 rates are 6.2–6.4 and energy rates are 5.8–6.0.

The key difference is algebraic structure rather than accuracy. BA variants produce square systems ($N_{\text{dof}} \times N_{\text{dof}}$, e.g., 13122×13122 on 81×81), directly compatible with standard sparse solvers. QR variants produce rectangular overdetermined systems (e.g., 13440×12800 for both NC-QR and SD-QR on 81×81) and require global least-squares treatment. Hence, BA matches QR accuracy while preserving a square-system structure.



(a) $p = 4$



(b) $p = 6$

Figure 4. Mixed Dirichlet–Neumann elasticity benchmark: NC-QR, NC-BA, SD-QR, SD-BA, and WG comparison in L^2 and energy norms for two polynomial orders. Strong-form variants impose Dirichlet data strongly, with Neumann handled by QR overdetermined enforcement or BA local absorption; WG uses Nitsche Dirichlet and natural Neumann treatment.

Table 7. Mixed-boundary elasticity benchmark: fitted convergence orders from the last three mesh levels. Both L^2 and energy rates are reported for $p = 4$ and $p = 6$, together with reference optimal rates, global system type, and system size on the 81×81 mesh.

| Method | L^2 ($p = 4/p = 6$) | Energy ($p = 4/p = 6$) | Opt. L^2 ($p+1$) | Opt. Energy (p) | System type | Size (81×81) |
|--------|-------------------------|--------------------------|----------------------|---------------------|-------------|-------------------------|
| NC-BA | 3.8 / 6.3 | 4.1 / 5.8 | 5 / 7 | 4 / 6 | square | 13122×13122 |
| NC-QR | 3.8 / 6.4 | 3.9 / 6.0 | 5 / 7 | 4 / 6 | rectangular | 13440×12800 |
| SD-BA | 4.0 / 6.2 | 4.2 / 5.9 | 5 / 7 | 4 / 6 | square | 13122×13122 |
| SD-QR | 3.7 / 6.2 | 3.9 / 6.0 | 5 / 7 | 4 / 6 | rectangular | 13440×12800 |
| WG | 5.8 / 7.9 | 4.4 / 6.6 | 5 / 7 | 4 / 6 | square | 13122×13122 |

8.4.2 DOF-based results for MiGFEM, standard p -FEM, and PUFEM

Objective. To provide a DOF-normalized comparison of three weak-form discretizations on the same smooth benchmark: MiGFEM WG ($p = 4$, $s = 3$), standard P_4 p -FEM, and classical PUFEM with degree-4 polynomial enrichment. The comparison emphasizes accuracy, conditioning, and runtime at comparable DOF scales.

Setup. We reuse the benchmark field (63) on $\Omega = (0, 5)^2$ and the structured mesh sequence 11×11 , 21×21 , 41×41 , 81×81 . MiGFEM WG uses CWLS degree $p = 4$, layer depth $s = 3$, and symmetric Nitsche Dirichlet treatment; the vector-form global system is solved directly and vector DOFs are reported. The p -FEM reference uses standard P_4 Lagrange triangles with strong Dirichlet imposition on all vector DOFs (vertex/edge/interior). PUFEM uses degree-4 enrichment on linear FE hats and symmetric penalty enforcement ($\beta = \mathcal{O}(E/h)$) for enriched boundary DOFs. Because boundary treatments differ (strong for p -FEM versus weak/penalty for MiGFEM WG and PUFEM), absolute constants are interpreted as controlled within-setting comparisons rather than strict one-to-one constants. For each method, we report displacement L^2 error, stress-based energy error, diagonal conditioning proxy $\kappa_{\text{diag}}(K) \approx \max(\text{diag}(K))/\min(\text{diag}(K))$, and total runtime (for MiGFEM and p -FEM) from the same execution script.

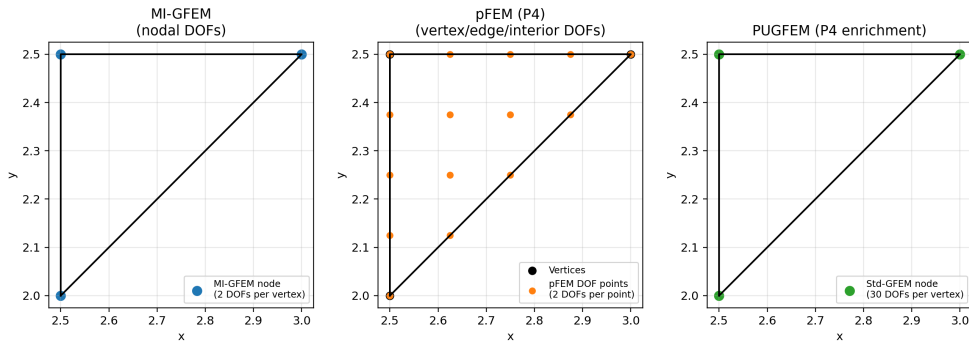


Figure 5. Illustration of DOF layouts for MiGFEM WG (nodal DOFs), standard P_4 p -FEM (vertex/edge/interior DOFs), and PUFEM (enriched nodal DOFs) on a representative triangle.

Results. Table 8 (representative mesh levels) and Figure 6 (error versus DOF trends) summarize the comparison. On 11×11 , L^2 errors span roughly $\mathcal{O}(10^{-3})$ to $\mathcal{O}(10^{-6})$ with DOFs from $\mathcal{O}(10^2)$ to $\mathcal{O}(10^3)$; on 81×81 , all three methods reach 10^{-8} – 10^{-11} in L^2 . At comparable DOF levels in this benchmark, MiGFEM shows favorable error levels relative to same-order p -FEM; this is reported as an empirical observation under the present discretization and boundary-treatment settings. All trends for L^2 , energy error, and conditioning proxy are provided directly in the table/figure set.

Table 8. Weak-form elasticity on $(0,5)^2$ with $p = 4$: MiGFEM WG, standard p -FEM, and PUFEM on structured meshes.

| Mesh | Method | N_{dof} | $\ \mathbf{u} - \mathbf{u}^h\ _{L^2}$ | $\ \mathbf{u} - \mathbf{u}^h\ _E$ | $\kappa_{\text{diag}}(K)$ | t_{total} (s) | $t_{\text{total}}/1000N_{\text{dof}}$ (s) |
|----------------|----------|------------------|---------------------------------------|-----------------------------------|---------------------------|------------------------|---|
| 11×11 | MiGFEM | 242 | 2.763×10^{-3} | 8.486×10^{-3} | 3.748×10^3 | 5.96 | 24.6 |
| | p -FEM | 3362 | 3.011×10^{-6} | 7.460×10^{-5} | 8.440 | 3.51 | 1.04 |
| | PUFEM | 3630 | 3.540×10^{-6} | 7.525×10^{-5} | 2.682×10^{14} | 8.66 | 2.39 |
| 21×21 | MiGFEM | 882 | 3.953×10^{-5} | 2.987×10^{-4} | 3.748×10^3 | 3.34 | 3.79 |
| | p -FEM | 13122 | 9.511×10^{-8} | 4.700×10^{-6} | 8.440 | 9.54×10^1 | 7.27 |
| | PUFEM | 13230 | 6.492×10^{-7} | 3.285×10^{-5} | 6.866×10^{16} | 2.91×10^1 | 2.20 |
| 41×41 | MiGFEM | 3362 | 6.881×10^{-7} | 1.362×10^{-5} | 3.748×10^3 | 1.24×10^1 | 3.69 |
| | p -FEM | 51842 | 2.980×10^{-9} | 2.944×10^{-7} | 8.440 | 2.30×10^2 | 4.44 |
| | PUFEM | 50430 | 1.356×10^{-6} | 1.403×10^{-4} | 1.758×10^{19} | 4.07×10^2 | 8.06 |
| 81×81 | MiGFEM | 13122 | 1.406×10^{-8} | 7.408×10^{-7} | 3.748×10^3 | 1.79×10^2 | 13.7 |
| | p -FEM | 206082 | 9.318×10^{-11} | 1.841×10^{-8} | 8.440 | 2.96×10^3 | 14.4 |
| | PUFEM | 196830 | 2.465×10^{-7} | 5.589×10^{-5} | 4.500×10^{21} | 1.71×10^3 | 8.68 |

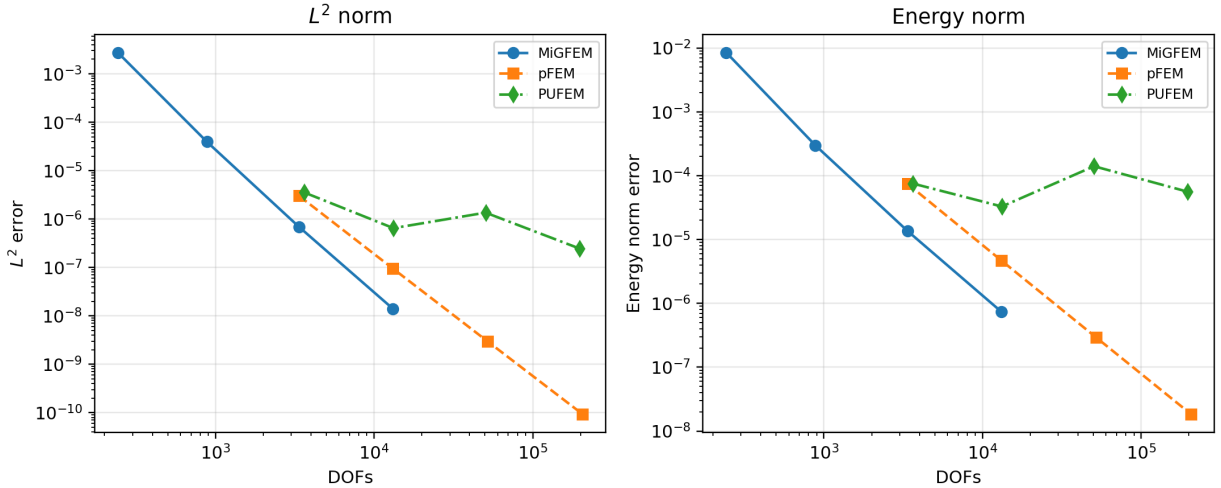


Figure 6. DOF-based comparison of MiGFEM WG, standard p -FEM, and PUFEM on $(0,5)^2$ with $p = 4$. Left: L^2 error versus total vector DOFs. Right: energy-norm error versus total vector DOFs.

A common formal convergence order is observed for this smooth case; differences are primarily tied to how polynomial content is distributed (element-interior for p -FEM versus patch/enrichment regions for MiGFEM and PUFEM). MiGFEM avoids extra element-interior unknowns, but this structural advantage is offset in part by patch-reconstruction cost per DOF (Table 8). In conditioning, the diagonal proxy remains moderate for MiGFEM, is smallest for p -FEM, and becomes extremely large for unstabilized PUFEM. The contrast highlights the difference between shared-data reconstruction (MiGFEM) and independent enrichment (PUFEM), while noting that stabilized GFEM variants (e.g., SGFEM [46]) can effectively mitigate enrichment ill-conditioning.

8.4.3 Conditioning study: scaling with mesh refinement

Objective. To quantify how algebraic conditioning scales with refinement for MiGFEM variants (NC/CC/SD/WG) relative to standard C^0 FEM and P_4 p -FEM under the same elasticity benchmark.

Setup. Using the benchmark in Section 8.4.2, we assemble matrices on 11×11 , 21×21 , and 41×41 meshes for: (i) MiGFEM NC/CC/SD and MiGFEM WG ($p = 4, s = 3$), (ii) FEM P_1 , and (iii) FEM P_4 . To reduce sensitivity to rigid-body modes and boundary-penalty terms, we evaluate conditioning on the interior block after consistent Dirichlet elimination:

$$\kappa_2(K_{II}) = \frac{\lambda_{\max}(K_{II})}{\lambda_{\min}(K_{II})},$$

using either direct evaluation or a sparse estimate as a proxy. Slopes are fitted from $\log \kappa_2$ versus $\log N_{\text{dof}}$.

Expected behavior. For second-order elliptic problems in 2D, one expects $\kappa_2(K_{II}) \sim \mathcal{O}(h^{-2})$, i.e., approximately linear growth with interior DOFs; high-order spaces typically change prefactors more than slopes.

Table 9. Conditioning data for the elasticity benchmark on $(0,5)^2$ (interior block K_{II}).

| Mesh | h | MiGFEM-NC | MiGFEM-CC | MiGFEM-SD | MiGFEM-WG | FEM P_1 | FEM P_4 |
|----------------|--------|--------------------|--------------------|--------------------|--------------------|--------------------|--------------------|
| 11×11 | 0.5000 | 4.04×10^1 | 5.63×10^1 | 5.74×10^1 | 6.04×10^1 | 6.22×10^1 | 3.15×10^3 |
| 21×21 | 0.2500 | 1.67×10^2 | 2.31×10^2 | 2.35×10^2 | 2.49×10^2 | 2.52×10^2 | 1.26×10^4 |
| 41×41 | 0.1250 | 6.73×10^2 | 9.30×10^2 | 9.46×10^2 | 1.01×10^3 | 1.01×10^3 | 5.04×10^4 |

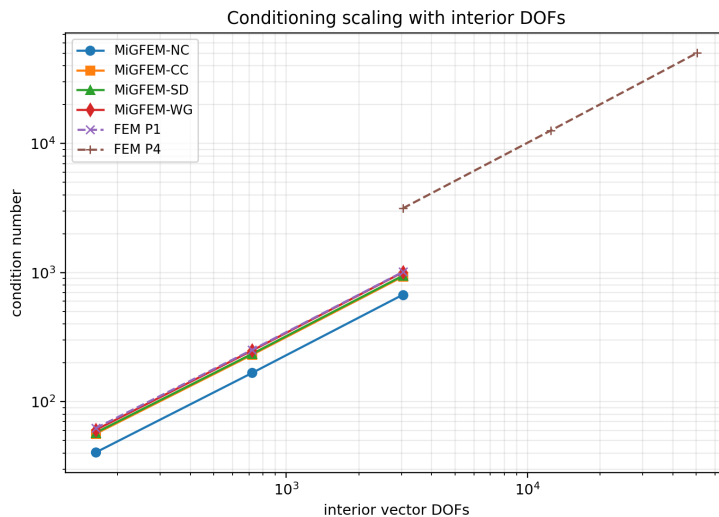


Figure 7. Conditioning against interior vector DOFs for MiGFEM (NC/CC/SD/WG), FEM P_1 , and FEM P_4 .

Results. Table 9 and Figure 7 show consistent monotone growth across all methods. On the 41×41 mesh, MiGFEM variants and FEM P_1 are at $\mathcal{O}(10^3)$, while FEM P_4 reaches 5.04×10^4 . Fitted slopes over the three-level sequence remain close to 1 (about 0.94–0.99) for MiGFEM and FEM references. Given the short sequence, slope estimates are indicative rather than definitive; nevertheless, the near-linear log–log trends are clear. In this dataset, inter-method differences are dominated by prefactors rather than slope changes.

8.4.4 Sensitivity to mesh perturbations in elasticity

Objective. To evaluate robustness of MiGFEM strong- and weak-form elasticity discretizations under mesh irregularity.

Setup. We again use (63) on $\Omega = (0,5)^2$. Starting from a structured 11×11 triangulation, interior nodes are randomly perturbed by $\delta \in \{0.3h, 0.5h\}$ while boundary nodes are fixed, producing irregular but shape-regular meshes (Figure 8). The same perturbation strategy is applied on all refinement levels up to 81×81 . We compare MiGFEM NC/CC/SD (strong form with intrinsic derivatives), MiGFEM WG (symmetric Nitsche), and standard weak-form P_4 p -FEM with exact Dirichlet imposition. Metrics are DOF-based L^2 and energy errors (Figures 9 and 10).

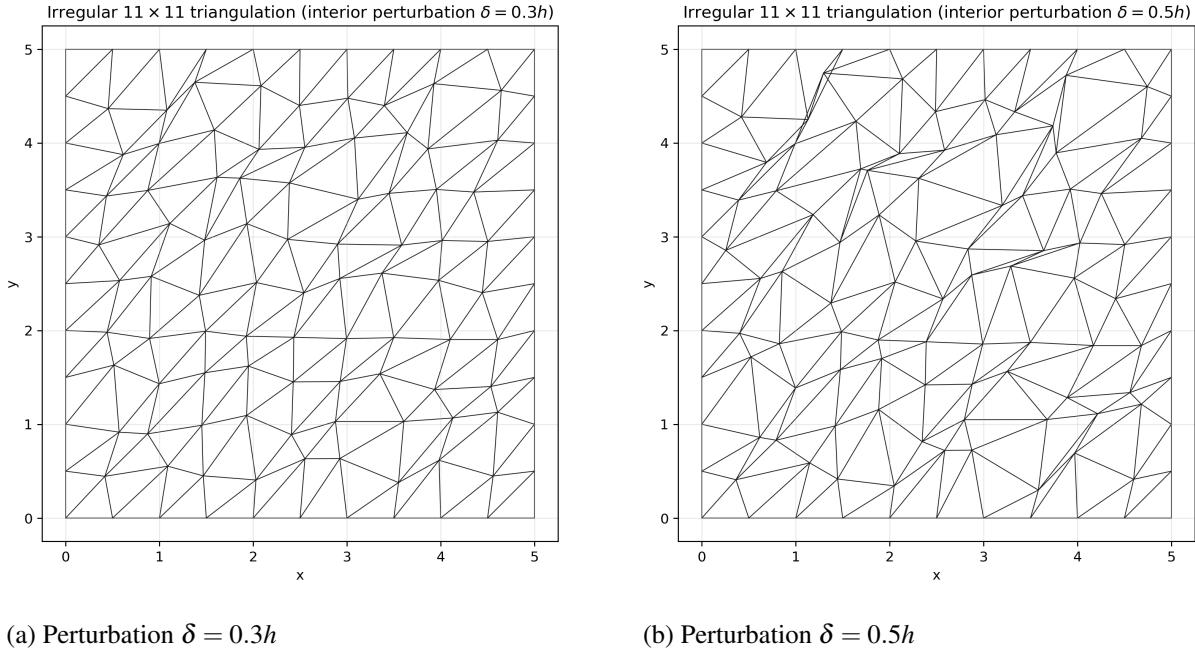


Figure 8. Representative irregular 11×11 triangulations on $(0,5)^2$ obtained by perturbing interior nodes by fractions $\delta \in \{0.3h, 0.5h\}$ of the local mesh size while keeping boundary nodes fixed.

Results. Across perturbed meshes, all MiGFEM variants retain monotone convergence in L^2 , H^1 , and energy norms. NC/CC/SD and WG remain stable over the tested distortion levels, indicating robust CWLS reconstruction under these perturbations. In this study, MiGFEM WG tracks the p -FEM weak-form reference closely, while strong-form variants show limited sensitivity to distortion in the reported error norms. This supports the subsequent, more focused strong-form irregular-mesh assessment in the biharmonic section.

8.4.5 WG post-processing: intrinsic vs. Leibniz derivatives

Objective. To verify whether replacing Leibniz derivatives by intrinsic derivatives in WG post-processing changes asymptotic error behavior.

Setup. Using the same smooth elasticity benchmark and mesh-refinement sequence, we compute WG energy-type post-processing errors with two derivative evaluations: (i) standard Leibniz derivatives, and (ii) intrinsic derivatives. We report results for $p = 1, 2, 4$.

Results. Figure 11 shows that the two derivative evaluations follow the same asymptotic convergence order across all tested polynomial degrees. For low-order cases ($p = 1, 2$), visible constant-level gaps appear on coarse meshes and decrease under refinement; for $p = 4$, the two curves are nearly indistinguishable over the

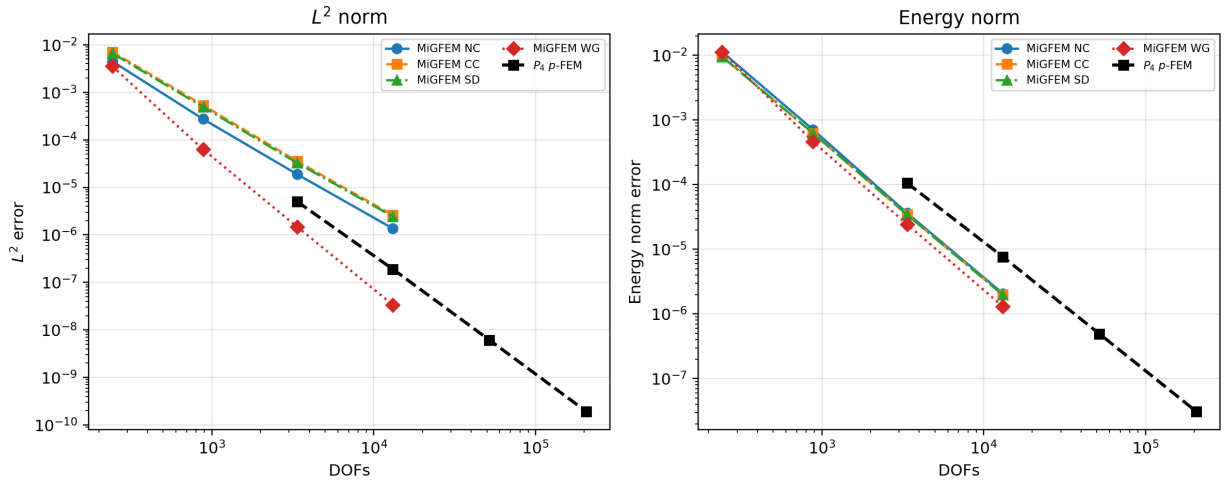


Figure 9. Elasticity benchmark on perturbed meshes with $\delta = 0.3h$: DOF-based L^2 and energy-norm errors for MiGFEM NC/CC/SD strong-form discretizations, MiGFEM WG, and P_4 p -FEM.

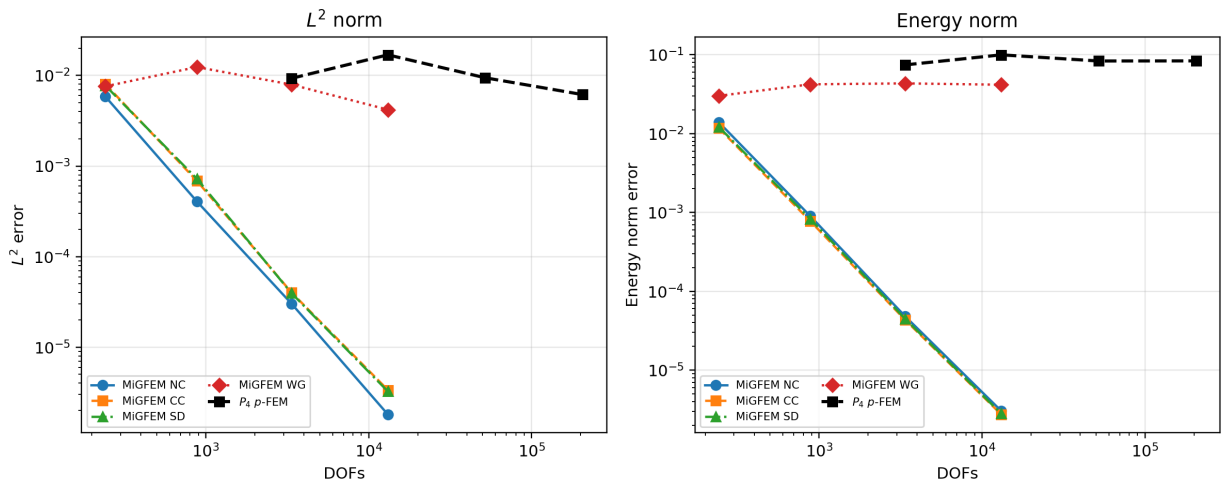


Figure 10. Elasticity benchmark on perturbed meshes with increased distortion ($\delta = 0.5h$): DOF-based L^2 and energy-norm errors for MiGFEM NC/CC/SD, MiGFEM WG, and P_4 p -FEM.

tested range. These results support that intrinsic differentiation introduces no additional order loss in WG post-processing, while directly providing smooth stress/strain fields for post-processing without separate recovery.

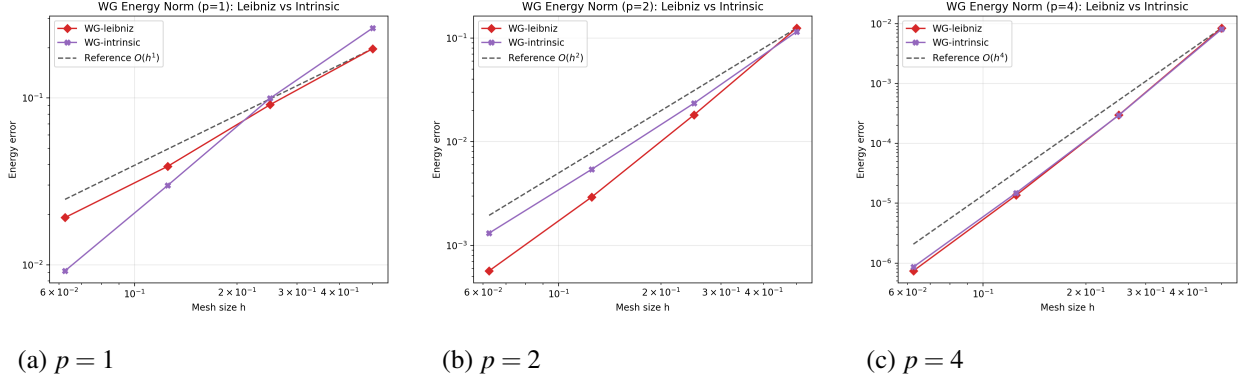


Figure 11. WG post-processing comparison of Leibniz and intrinsic derivatives for $p = 1, 2, 4$. Both derivative evaluations show the same asymptotic order; differences are mainly in pre-asymptotic constants, especially for low p .

8.5 Performance on Fourth-Order PDEs: Biharmonic Equation

We now assess MiGFEM on a representative fourth-order problem, $\Delta^2 u = f$, with emphasis on three tightly connected questions: (i) how much accuracy is already present in the approximation space, (ii) how this accuracy transfers to full strong-form solves (NC/CC/SD), and (iii) whether the BA-CWLS boundary treatment remains stable on strongly distorted meshes. The subsection is organized accordingly, using one unified benchmark throughout to ensure comparability.

8.5.1 Problem setting and error measures

We consider the biharmonic benchmark on $\Omega = (0, 1)^2$:

$$\begin{aligned}
 \Delta^2 u &= f & \text{in } \Omega, \\
 \mathcal{B}_1 u &= \bar{g}_1 & \text{on } \partial\Omega, \\
 \mathcal{B}_2 u &= \bar{g}_2 & \text{on } \partial\Omega,
 \end{aligned} \tag{64}$$

with clamped boundary data $(u, \partial_n u)$ generated from the manufactured solution $u(x, y) = \sin(\pi x) \sin(\pi y)$, yielding $f = 4\pi^4 \sin(\pi x) \sin(\pi y)$. Because this solution is smooth and symmetric on a convex domain, it provides a clean setting to examine discretization behavior without corner singularity effects.

The mesh sequence is uniformly refined, and interior nodes are perturbed by $\delta \in \{0.0h, 0.5h, 0.8h, 1.0h\}$, covering regular to strongly distorted triangulations (Figure 12). Errors are measured by the element-integrated norms $\|e\|_{L_h^2}$ and $|e|_{H_h^2}$, where derivatives are evaluated intrinsically from the CWLS reconstruction at quadrature points. For direct comparison across mesh levels, we report normalized values $\|e\|_{L_h^2}/|\Omega|^{1/2}$ and $|e|_{H_h^2}/|\Omega|^{1/2}$.

For the three strong-form variants, NC enforces the PDE at interior nodes, SD uses nodal-star averaging, and CC enforces at element centroids with global least-squares enforcement. Dirichlet values are imposed strongly by boundary-node elimination, while the derivative boundary condition is imposed through BA-CWLS local absorption. Under this unified formulation setting, the subsequent nodal-injection and full-solve diagnostics can be interpreted consistently in terms of approximation-space versus global-discretization effects.

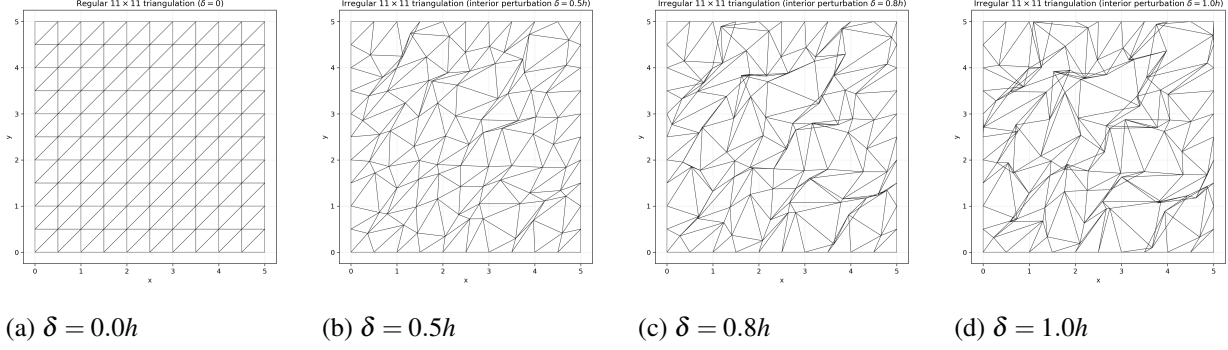


Figure 12. Representative 11×11 meshes for the biharmonic benchmark with perturbation levels $\delta = 0.0h, 0.5h, 0.8h, 1.0h$.

8.5.2 Approximation-space diagnostic: exact nodal injection

Objective. To isolate the approximation-space capability from algebraic solve and boundary-enforcement effects.

Setup. We inject exact nodal values of the analytical solution. NC/CC/SD therefore share the same reconstructed field, and the measured errors become collocation-independent indicators of interpolation quality.

Results. Figures 13 and 14 show monotone decay of both L^2 and H^2 errors for $p = 4$ and $p = 6$. On regular meshes, observed slopes align with CWLS interpolation expectations (roughly $L^2 \sim p + 1$, $H^2 \sim p - 1$). Under strong distortion ($\delta = 1.0h$), asymptotic rates are largely preserved while constants increase, indicating that distortion mainly affects local conditioning/stencil anisotropy rather than approximation order, provided patches remain unisolvent. This also confirms that intrinsic derivative evaluation does not add extra order loss for smooth fields (cf. Eq. (25)).

8.5.3 Full-system strong-form convergence and boundary robustness

Objective. To evaluate how approximation-space quality transfers to full NC/CC/SD solves, and to verify stability of BA-CWLS boundary absorption under distortion.

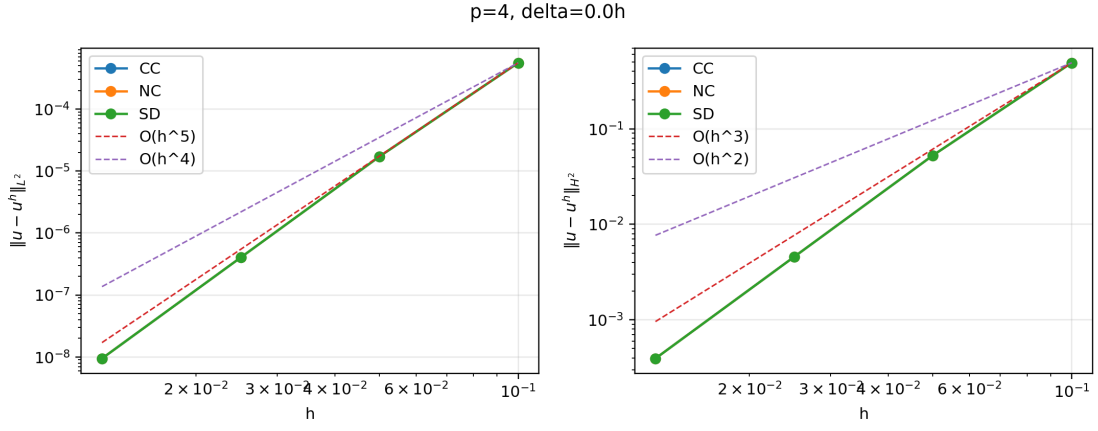
Setup. We solve the assembled global systems with the same PDE, mesh families, and norms as above. NC is pointwise nodal collocation, SD uses nodal-star averaging, and CC is overdetermined centroid collocation solved by least squares. For all three, $u = \bar{g}_1$ is imposed strongly and $\partial_n u = \bar{g}_2$ is imposed by BA-CWLS.

Results. Figures 15–16 show stable, monotone convergence on both regular and perturbed meshes. For $p = 4$, fitted L_h^2 rates are about 1.6–1.7 on regular meshes and remain comparable under $\delta = 1.0h$, with increased constants. For $p = 6$, NC/CC/SD exhibit higher-order decay (about 3.3–3.6 on regular meshes), with moderate slope reduction but no qualitative instability under strong perturbation.

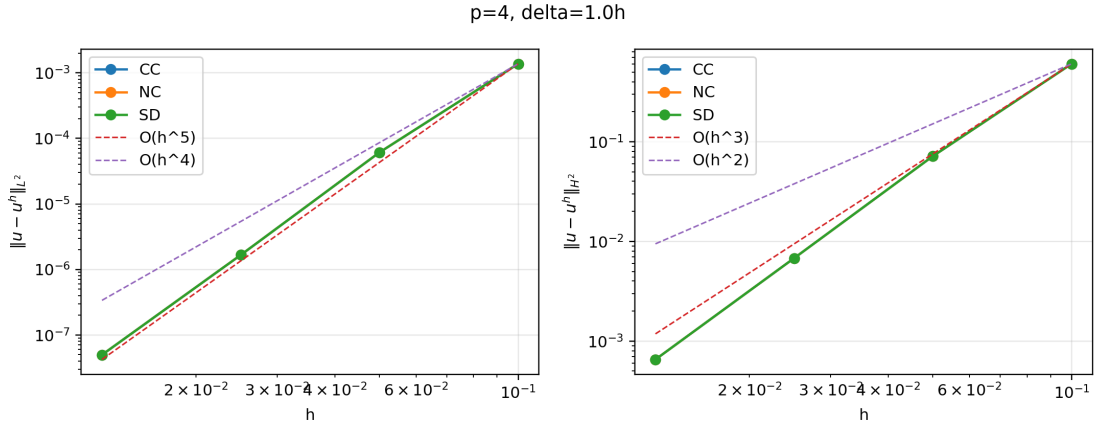
The observed full-solve L^2 behavior (roughly $p - 2$) is lower than the interpolation-optimal $p + 1$ seen in nodal injection. Combined diagnostics indicate this is not caused by trial-space quality or boundary enforcement: (1) nodal injection confirms optimal approximation-space rates, and (2) BA-versus-penalty comparisons in Section 9 show essentially unchanged slopes. (3) The remaining limiter is the consistency of pointwise strong-form collocation for fourth-order PDEs.

To connect these trends with BA-CWLS theory, Table 10 reports admissibility indicators. Small absorption ratios $\eta \ll 1$, controlled local KKT conditioning K , and near-machine-zero consistency/transfer residuals confirm stable and polynomial-consistent boundary absorption over the full refinement sequence.

Diagnostic note on conditioning. At higher polynomial degree (e.g., $p = 6$), large local K values mainly reflect known growth of polynomial least-squares conditioning and KKT amplification. The key observation



(a) $p = 4$, regular mesh ($\delta = 0.0h$)

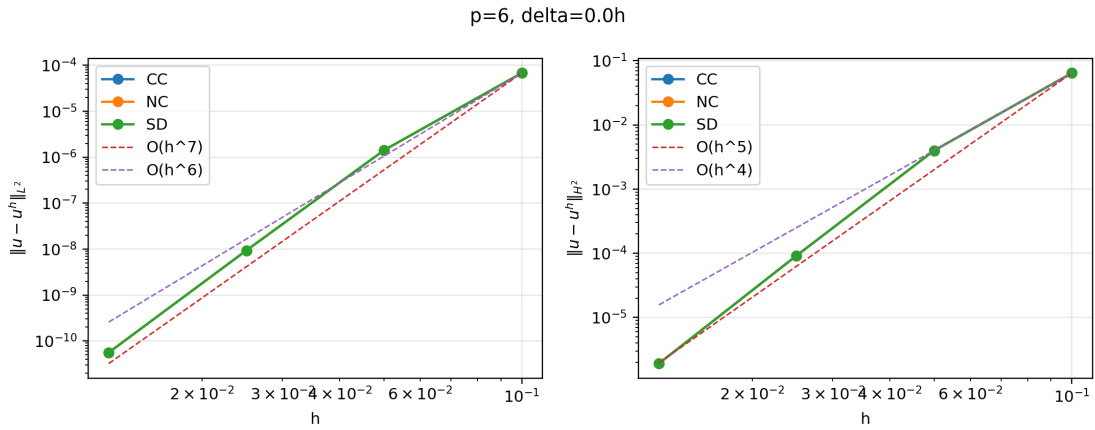


(b) $p = 4$, strong perturbation ($\delta = 1.0h$)

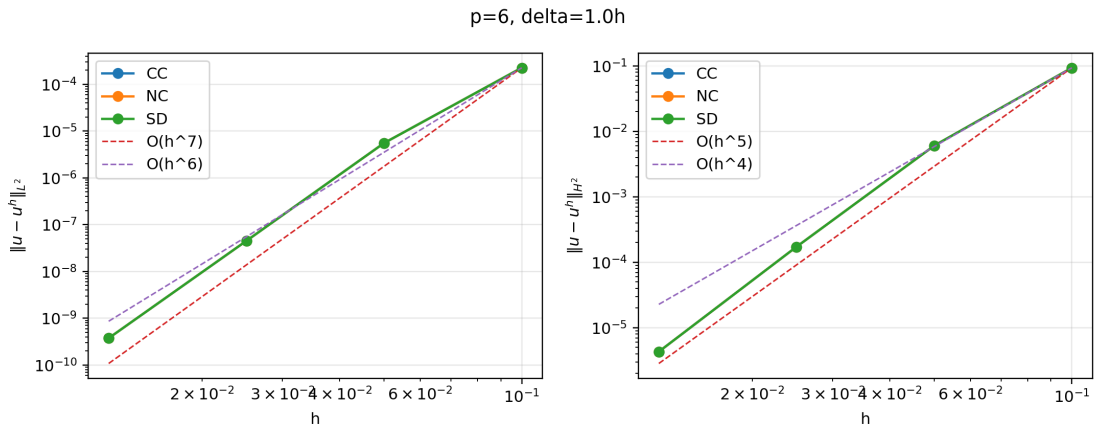
Figure 13. Nodal-injection diagnostic for the biharmonic benchmark at $p = 4$.

Table 10. BA-CWLS admissibility indicators on regular and strongly perturbed meshes.

| (p, δ) | η (mean) | K | $\mathcal{E}_{\text{poly},dn}^{\text{RMS}}$ | $\mathcal{E}_{dn,\partial\Omega}^{\text{RMS}}$ | $\mathcal{E}_{\text{poly},dn}^{\text{max}}$ |
|---------------|---------------|--------------------|---|--|---|
| (4, 0.0h) | 0.200 | 6.42×10^5 | 3.34×10^{-14} | 2.38×10^{-15} | 1.32×10^{-13} |
| (4, 1.0h) | 0.200 | 9.59×10^5 | 1.95×10^{-14} | 4.64×10^{-15} | 2.66×10^{-13} |
| (6, 0.0h) | 0.107 | 1.96×10^9 | 1.58×10^{-13} | 2.40×10^{-14} | 8.91×10^{-13} |
| (6, 1.0h) | 0.107 | 1.95×10^9 | 2.08×10^{-13} | 6.90×10^{-14} | 1.74×10^{-12} |



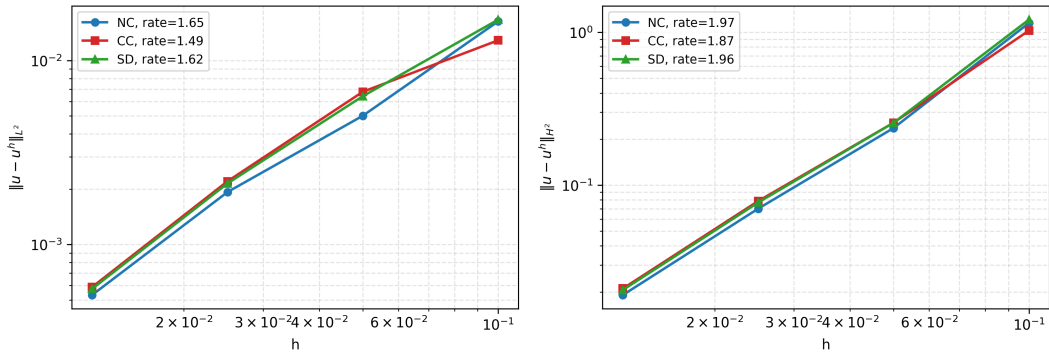
(a) $p = 6$, regular mesh ($\delta = 0.0h$)



(b) $p = 6$, strong perturbation ($\delta = 1.0h$)

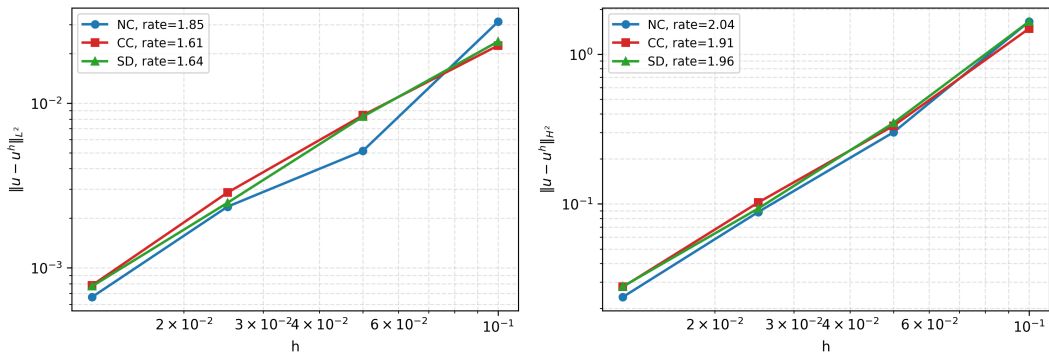
Figure 14. Nodal-injection diagnostic for the biharmonic benchmark at $p = 6$.

Integrated error norms: $p=4, \delta=0.0h$



(a) $p = 4, \delta = 0.0h$

Integrated error norms: $p=4, \delta=1.0h$



(b) $p = 4, \delta = 1.0h$

Figure 15. Full-solve convergence for biharmonic NC/CC/SD at $p = 4$.

is that these values are nearly refinement-independent, while consistency and boundary-transfer residuals remain near machine precision. In practice, this indicates numerically stable BA-CWLS operation in the tested regime.

Remark 1 (Observed order gap in strong-form fourth-order solves). *The benchmark consistently shows a gap between the interpolation-optimal behavior observed under nodal injection and the full-solve rates obtained from the strong-form discretization. For the present biharmonic setting, the empirical full-solve L^2 convergence is approximately $p - 2$, whereas nodal injection recovers the interpolation-optimal $p + 1$ behavior. The combined diagnostics indicate that this gap is not caused by trial-space quality or by boundary enforcement. First, nodal injection confirms that the approximation space attains the optimal rate. Second, the BA-versus-penalty comparison in Section 9 yields essentially unchanged slopes. The remaining limiter is therefore attributed to the consistency of pointwise strong-form collocation for fourth-order PDEs. Even with this order gap, the method retains monotone convergence throughout the tested mesh sequence.*

Independently of this order gap, robustness under severe distortion, including geometrically inverted elements, follows from the physical-space construction of CWLS and PoU. Because the reconstruction is carried out directly in global coordinates, the basis definition does not require an isoparametric Jacobian. Accordingly, as long as the local patches remain unisolvent and the element areas remain nonzero, NC/CC/SD retain stable approximation and convergence behavior in this benchmark.

9 Numerical Comparison in MiGFEM-NC: CWLS vs RBF

For primal strong-form discretization of high-order PDEs, RBF-FD-type local approximation is widely used. This section compares CWLS- and RBF-based local reconstructions *within the same* MiGFEM-NC strong-form framework. The purpose is to isolate the influence of local approximation and boundary closure without changing the global collocation machinery. In all runs, governing equation, collocation layout, mesh sequence, and error definitions are identical; only the local reconstruction and derivative-boundary treatment are changed.

Three variants are considered:

- **CWLS-BA**: polynomial CWLS with local BA absorption of derivative-boundary constraints;
- **CWLS-Penalty**: polynomial CWLS with global penalty enforcement;
- **RBF-Penalty**: PHS-RBF reconstruction with the same global penalty enforcement.

The benchmark is the manufactured biharmonic problem on $(0, 1)^2$,

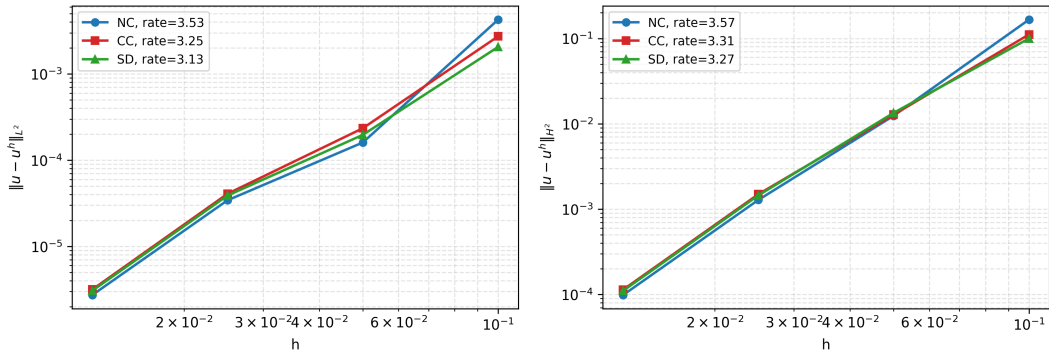
$$u(x, y) = \sin(\pi x) \sin(\pi y), \quad f = 4\pi^4 \sin(\pi x) \sin(\pi y),$$

solved on meshes from 11×11 to 161×161 . Dirichlet values are imposed strongly at boundary nodes for all variants. For derivative-type boundary conditions, CWLS-Penalty and RBF-Penalty use global penalty enforcement, while CWLS-BA uses the local absorption mechanism in (39)–(45).

Figures 17 and 18 report convergence in $\|e\|_{L_h^2}$ and $|e|_{H_h^2}$ for $p = 4$ and $p = 6$. Figures 19 and 20 compare conditioning and total runtime. Table 11 summarizes representative cross-mesh values for CWLS-Penalty and CWLS-BA, including H^2 errors, conditioning indicators, and boundary residuals.

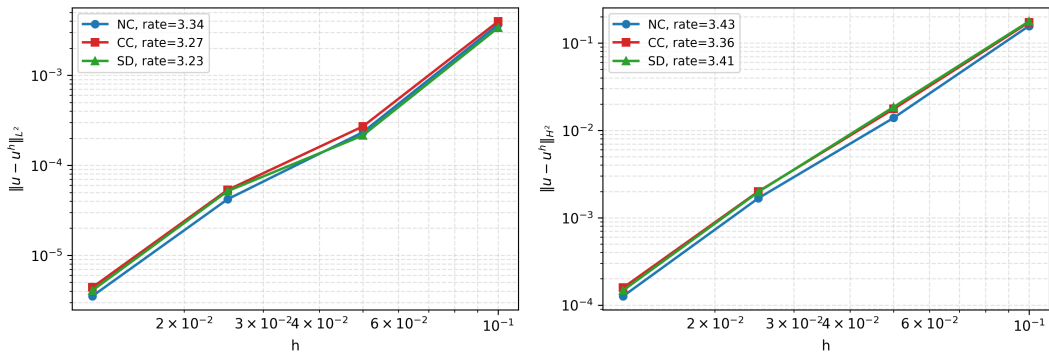
The numerical trends indicate a clear accuracy–conditioning–cost trade-off. RBF-Penalty generally achieves smaller error constants at comparable mesh levels, but its runtime is higher and fine-mesh rate behavior is less uniform than CWLS-based variants. Between the two CWLS enforcement strategies, BA and penalty give similar asymptotic convergence behavior, but BA yields systematically better matrix conditioning and faster solves. In this dataset, the conditioning proxy scales approximately as $\kappa_{\text{diag}} \sim h^{-4}$ for

Integrated error norms: $p=6, \delta=0.0h$



(a) $p = 6, \delta = 0.0h$

Integrated error norms: $p=6, \delta=1.0h$



(b) $p = 6, \delta = 1.0h$

Figure 16. Full-solve convergence for biharmonic NC/CC/SD at $p = 6$.

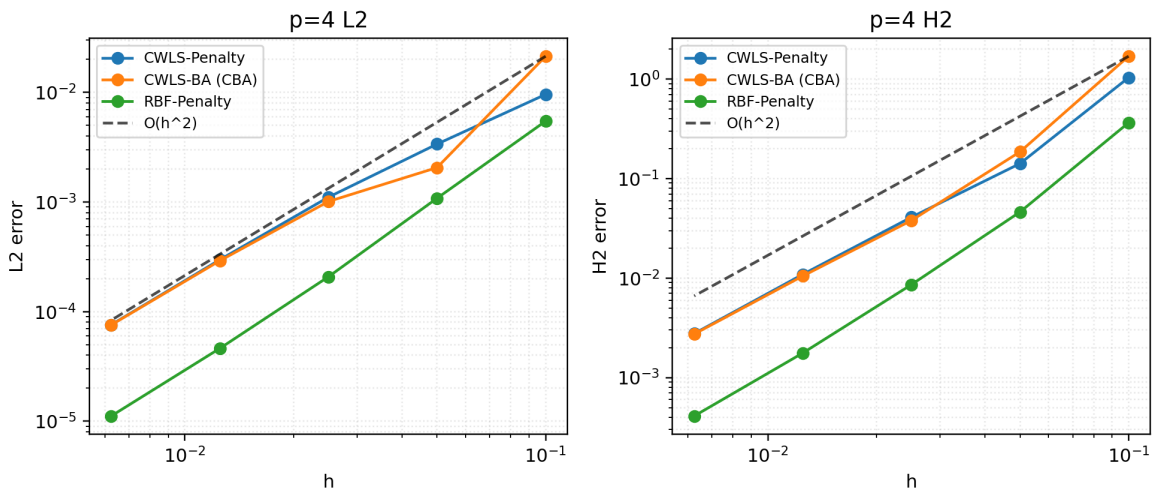


Figure 17. NC biharmonic comparison for $p = 4$: CWLS-Penalty, CWLS-BA, and RBF-Penalty. Dashed reference line: $O(h^2)$.

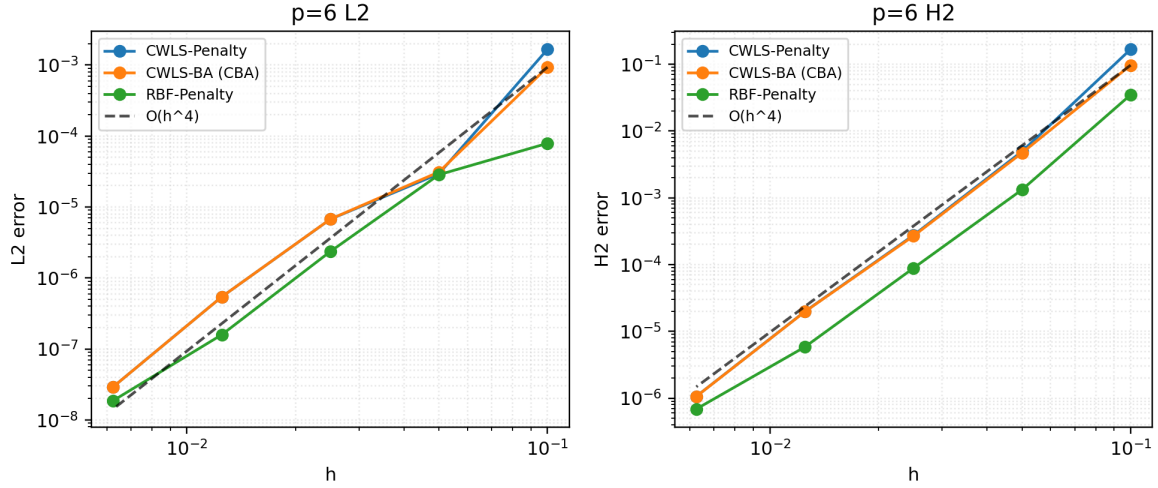


Figure 18. NC biharmonic comparison for $p = 6$: CWLS-Penalty, CWLS-BA, and RBF-Penalty. Dashed reference line: $O(h^4)$.

Table 11. Benchmark comparison (CWLS-Penalty vs CWLS-BA): global conditioning and boundary-condition satisfaction across mesh levels.

| p | mesh | H^2 (Penalty) | H^2 (BA) | $\kappa_{\text{diag}}(A)$ (Penalty) | $\kappa_{\text{diag}}(A)$ (BA) | BC residual $\varepsilon_{dn,\partial\Omega}^{\text{RMS}}$ (Penalty / BA) |
|-----|------------------|------------------------|------------------------|-------------------------------------|--------------------------------|---|
| 4 | 21×21 | 1.414×10^{-1} | 1.855×10^{-1} | 6.872×10^6 | 2.195×10^5 | $6.583 \times 10^{-4} / 1.926 \times 10^{-15}$ |
| | 41×41 | 4.089×10^{-2} | 3.787×10^{-2} | 2.224×10^8 | 3.513×10^6 | $1.456 \times 10^{-5} / 3.642 \times 10^{-15}$ |
| | 81×81 | 1.090×10^{-2} | 1.048×10^{-2} | 7.158×10^9 | 5.620×10^7 | $3.926 \times 10^{-7} / 1.054 \times 10^{-15}$ |
| | 161×161 | 2.768×10^{-3} | 2.734×10^{-3} | 2.297×10^{11} | 8.992×10^8 | $6.783 \times 10^{-9} / 1.114 \times 10^{-15}$ |
| 6 | 21×21 | 4.951×10^{-3} | 4.705×10^{-3} | 2.164×10^7 | 9.014×10^5 | $6.279 \times 10^{-5} / 2.865 \times 10^{-14}$ |
| | 41×41 | 2.747×10^{-4} | 2.678×10^{-4} | 7.069×10^8 | 1.442×10^7 | $6.246 \times 10^{-7} / 2.582 \times 10^{-14}$ |
| | 81×81 | 1.982×10^{-5} | 1.971×10^{-5} | 2.285×10^{10} | 2.308×10^8 | $1.167 \times 10^{-9} / 2.640 \times 10^{-14}$ |
| | 161×161 | 1.064×10^{-6} | 1.060×10^{-6} | 7.350×10^{11} | 3.692×10^9 | $4.925 \times 10^{-11} / 5.146 \times 10^{-15}$ |

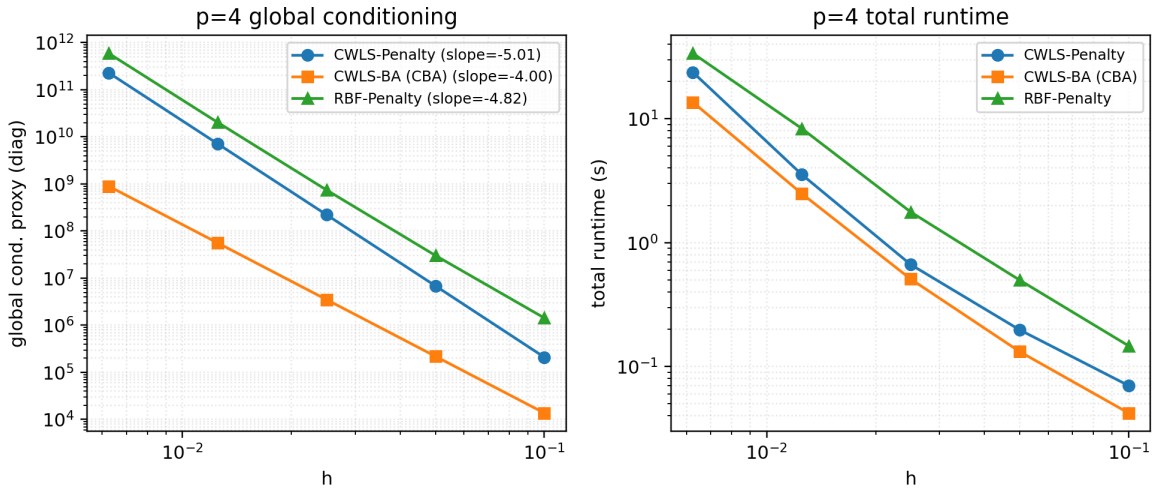


Figure 19. Global conditioning and total-runtime comparison for $p = 4$: CWLS-Penalty, CWLS-BA, and RBF-Penalty under the same MiGFEM-NC discretization setting. Left: global matrix conditioning proxy (diagonal-based). Right: total runtime versus mesh size.

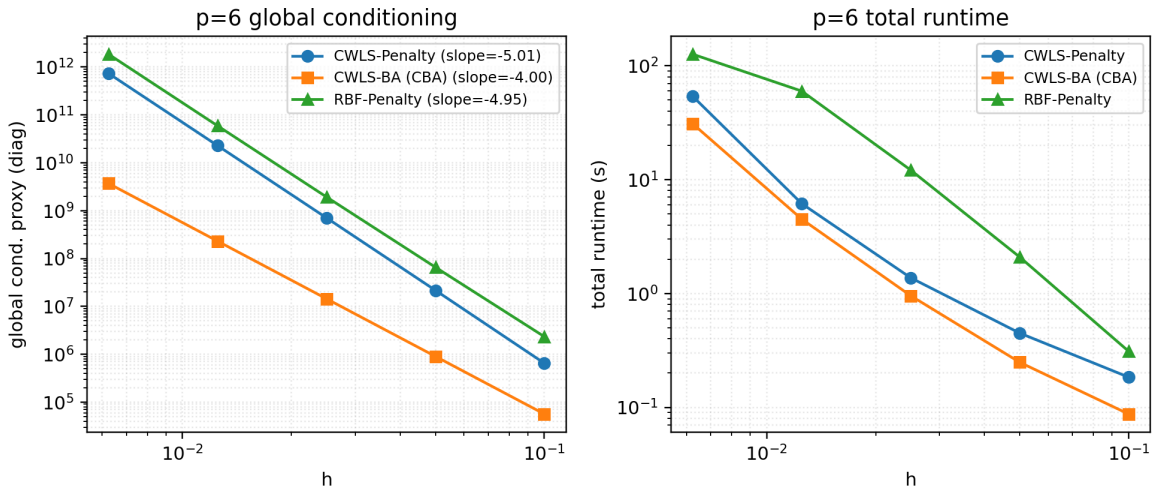


Figure 20. Global conditioning and total-runtime comparison for $p = 6$: CWLS-Penalty, CWLS-BA, and RBF-Penalty under the same MiGFEM-NC discretization setting. Left: global matrix conditioning proxy (diagonal-based). Right: total runtime versus mesh size.

CWLS-BA, versus $\sim h^{-5}$ for CWLS-Penalty and RBF-Penalty, indicating a one-order conditioning advantage for local absorption.

From a formulation viewpoint, this behavior is consistent with how BA is embedded in CWLS: absorbed constraints are incorporated locally through a structured KKT system, preserving a well-controlled polynomial reconstruction process. Although BA can in principle be extended to RBF reconstructions, the RBF setting is typically more sensitive to local ill-conditioning, so penalty enforcement remains the pragmatic baseline there.

Overall, within the same MiGFEM-NC framework, CWLS-BA offers the most balanced profile among the tested variants: near-competitive accuracy with substantially improved conditioning and reduced runtime.

10 Discussion and limitations

10.1 What is established in this study

The results across Sections 3–8 support a coherent picture of the proposed method. First, at the approximation-space level, the PoZ/interface-coherence mechanism is numerically confirmed: polynomial patch tests are satisfied to machine precision, and smooth nonpolynomial fields exhibit the predicted jump-decay law $\mathcal{O}(h^{p+1-|\alpha|})$. Second, at the derivative-evaluation level, the intrinsic derivative behaves as designed: it is polynomial-exact and consistency-preserving for smooth fields, so pointwise strong-form evaluation can be performed on standard C^0 meshes without introducing additional global DOFs. Third, at the discretization level, one mesh-intrinsic trial space supports both weak-form (WG) and strong-form (NC/CC/SD) realizations on the tested elasticity and biharmonic benchmarks.

For second-order elasticity, WG follows the expected variational trend, whereas the strong-form branches show a reproducible one-order reduction in the displacement L^2 convergence rate; within the strong-form branch, BA and QR treatments yield essentially the same errors and rates. The corresponding distinction between BA and QR is therefore algebraic (square sparse systems versus overdetermined least-squares systems) rather than accuracy-limiting in the tested regime. For fourth-order biharmonic problems, the full strong-form solves follow the same pattern: the observed L_h^2 convergence remains below nodal-injection interpolation behavior, indicating a consistency/stability limit of primal pointwise collocation rather than loss of polynomial reproduction in the reconstruction itself. In the same benchmark regime, BA-CWLS maintains boundary-condition fidelity while preserving a square sparse global algebraic structure.

10.2 Positioning relative to existing high-regularity technologies

Relative to classical C^1 elements, IGA, and meshfree/GFDM/RBF-FD families, MiGFEM occupies an intermediate position. It does not construct globally C^1 trial bases, and it does not add generalized enrichment DOFs. Instead, it uses nodal-patch reconstruction from shared nodal data plus PoU blending to obtain high-order derivative usability on top of standard C^0 meshes. In this sense, the method trades specialized global smooth basis construction for local reconstruction work, while retaining FEM-compatible sparsity, nodal unknown management, and assembly workflow.

Compared with stencil-only strong-form methods, MiGFEM-NC has the same local stencil algebra at nodes but additionally retains an explicit global trial field and PoZ-governed smoothness mechanism. This global structure is what connects local reconstruction consistency, jump behavior, and unified weak/strong discretization within a single framework.

10.3 Current limitations and open problems

Despite the encouraging results, several limitations remain.

1. **BA-CWLS analysis is not yet complete.** The present study shows that BA-CWLS preserves boundary-condition fidelity and the square sparse algebraic structure in the tested regime. A dedicated analysis

is still needed, however, to quantify how boundary sampling density, local constraint layout, patch geometry, and weighting choices affect conditioning, consistency, and robustness. A sharper understanding of BA-type absorption may help establish a practical strong-form formulation in which derivative-type boundary conditions are enforced exactly without sacrificing the square sparse algebraic structure.

2. **Parameter robustness is not fully mapped.** Although the tested CWLS/BA settings are robust, a systematic sensitivity map for (p, s) , weighting kernels, patch geometry, boundary sampling density, and solver/preconditioner coupling is still needed for production-level guidelines.
3. **Three-dimensional validation is pending.** The formulation is dimension-independent, but current evidence is predominantly 2D. Large-scale 3D verification is required, especially for complex boundary intersections, anisotropic meshes, and high-order derivative boundary constraints.
4. **Non-smooth fields remain a central challenge in strong form.** The PoZ smoothness-transfer argument relies on sufficiently smooth local behavior. Near singularities (re-entrant corners, crack tips, material interfaces), patch coherence deteriorates and direct strong-form collocation may lose robustness. Integrating singular enrichments—as in IXFEM-type weak-form practice [43, 44, 52, 53, 54, 61, 62, 63, 64, 65, 67]—with the present strong-form BA-CWLS scheme remains an important unresolved direction.
5. **Conditioning and scalability need further work at high order.** As p increases, local KKT conditioning and global system conditioning become more demanding. Matrix-free assembly, block preconditioning, and scalable parallel implementations are necessary for very large problem sizes.

11 Conclusions

This work develops a mesh-intrinsic GFEM for high-order PDEs on standard C^0 unstructured meshes, without introducing extra global DOFs. Local approximants are reconstructed on overlapping nodal patches from shared nodal data and blended by PoU, so high-order derivative capability is obtained through reconstruction/interface coherence rather than globally C^1 trial bases.

The core theoretical result is the PoZ-based smoothness-transfer mechanism: for polynomial reproduction, inter-element derivative jumps cancel exactly up to the reconstruction order; for smooth nonpolynomial fields, jumps decay as $\mathcal{O}(h^{p+1-|\alpha|})$. Based on this structure, the intrinsic derivative is polynomial-exact and approximation-order consistent, enabling pointwise strong-form evaluation on C^0 meshes. The same trial space supports both weak-form Galerkin and strong-form NC/CC/SD discretizations.

In strong-form collocation methods, the explicit enforcement of derivative-type and free-surface boundary conditions conventionally produces heavily overdetermined global systems, compromising both algebraic conditioning and solver efficiency. The proposed BA-CWLS algorithm circumvents this bottleneck by locally absorbing boundary constraints into the least-squares reconstruction phase. This strategy achieves exact, pointwise satisfaction of derivative-type boundary conditions without resorting to penalty parameters or expanding the global system size. As demonstrated in the two-dimensional benchmarks, this absorption mechanism robustly preserves a square, sparse algebraic structure and maintains boundary fidelity, while delivering convergence behavior comparable to overdetermined enforcement in the tested regime.

Numerical evidence is consistent with these claims in the tested regime: machine-precision patch tests, predicted jump-decay slopes, and robust performance on severely distorted meshes. WG follows the expected variational trend, whereas strong-form full solves for both second-order elasticity and fourth-order biharmonic problems show a reproducible reduction in the L^2 -type convergence order relative to interpolation-optimal nodal-injection behavior. This indicates that consistency/stability of pointwise primal collocation,

rather than loss of reconstruction polynomial exactness, remains the main limiting factor in the present formulation.

Overall, the weak-form branch of MiGFEM already exhibits several features that are directly relevant to mainstream CAE deployment: it avoids the classical linear-dependence difficulty associated with extra-DOF enrichments, combines locally meshfree reconstruction with a globally finite-element and interpolatory structure, retains polynomial shape functions that remain quadrature-friendly, and provides smooth stress/strain post-processing directly on standard C^0 meshes. Because these properties are obtained without departing from the nodal unknown management, sparse assembly pattern, and mesh infrastructure of conventional FEM, the formulation can in principle be integrated into existing industrial CAE workflows at low adoption cost and thus provides a practical basis for further engineering development. The strong-form branch also warrants further study because collocation retains intrinsic computational attractions, especially in reducing variational-form complexity and in simplifying model setup and boundary-data treatment at the preprocessing stage. Future work will proceed along two directions. For the weak-form branch, priority will be given to three-dimensional software development and engineering implementation on existing CAE platforms. For the strong-form branch, emphasis will be placed on identifying and exploiting its intrinsic advantages, particularly those related to preprocessing convenience, boundary treatment, and computational efficiency.

References

- [1] O.C. Zienkiewicz, R.L. Taylor. *The Finite Element Method: Its Basis and Fundamentals*, 7th ed., Butterworth-Heinemann, 2013.
- [2] K.J. Bathe. *Finite Element Procedures*, 2nd ed., Prentice Hall, 2014.
- [3] T.J.R. Hughes. *The Finite Element Method: Linear Static and Dynamic Finite Element Analysis*, Prentice-Hall International, Englewood Cliffs, New Jersey, 1987.
- [4] S.C. Brenner, L.R. Scott. *The Mathematical Theory of Finite Element Methods*, Springer, 2008.
- [5] A. Ern, J.-L. Guermond. *Theory and Practice of Finite Elements*, Springer, 2004.
- [6] S. Timoshenko, S. Woinowsky-Krieger. *Theory of Plates and Shells*, 2nd ed., McGraw-Hill, New York, 1959.
- [7] J.N. Reddy. *Theory and Analysis of Elastic Plates and Shells*, CRC Press, Taylor and Francis, 2007.
- [8] A.C. Eringen. *Nonlocal Continuum Field Theories*, Springer, New York, 2001.
- [9] R.D. Mindlin. Second gradient of strain and surface-tension in linear elasticity, *International Journal of Solids and Structures* 1 (1965) 417–438.
- [10] E.C. Aifantis. On the role of gradients in the localization of deformation and fracture, *International Journal of Engineering Science* 30 (1992) 1279–1299.
- [11] G. A. Maugin. *Non-Classical Continuum Mechanics: A Dictionary*, Springer, 2017.
- [12] C. Miehe, F. Welschinger, M. Hofacker. Thermodynamically consistent phase-field models of fracture: Variational principles and multi-field FE implementations, *International Journal for Numerical Methods in Engineering* 83 (2010) 1273–1311.
- [13] J.W. Cahn, J.E. Hilliard. Free energy of a nonuniform system. I. Interfacial free energy, *The Journal of Chemical Physics* 28 (1958) 258–267.

- [14] Liangzhe Zhang, M. R. Tonks, D. Gaston, J.W. Peterson, D. Andrs, P.C. Millett, B.S. Biner. A quantitative comparison between C^0 and C^1 elements for solving the Cahn–Hilliard equation, *Journal of Computational Physics* 236 (2013) 74–80.
- [15] H. Lamb. *Hydrodynamics*, 6th ed., Cambridge University Press, Cambridge, 1994.
- [16] R.W. Clough, J.L. Tocher. Finite Element Stiffness Matrices for Analysis of Plates in Bending, *Proceedings of the Conference on Matrix Methods in Structural Mechanics*, Wright-Patterson Air Force Base, 1965, pp. 515–545.
- [17] J.H. Argyris, I. Fried, D.W. Scharpf. The TUBA Family of Plate Elements for the Matrix Displacement Method, *Aeronautical Journal of the Royal Aeronautical Society*, 72(692), 1968: 701–709.
- [18] F.K. Bogner, R.L. Fox, L.A. Schmit. The Generation of Interelement Compatible Stiffness and Mass Matrices by the Use of Interpolation Formulas, Wright-Patterson Air Force Base, Ohio, 1965, pp. 395–443.
- [19] M. Zlámal. The Finite Element Method in Domains with Curved Boundaries, *International Journal for Numerical Methods in Engineering* 5(3) (1973) 367–373.
- [20] P.G. Ciarlet, P.A. Raviart. Interpolation Theory over Curved Elements, with Applications to Finite Element Methods, *Computer Methods in Applied Mechanics and Engineering* 1(2) (1972) 217–249.
- [21] P.G. Ciarlet. *The Finite Element Method for Elliptic Problems*, North-Holland, Amsterdam, 2012.
- [22] Rong Tian, A GFEM with C^1 -continuity, *Chinese Journal of Theoretical and Applied Mechanics* 51 (1) (2019) 263–277. DOI: 10.6052/0459-1879-18-188.
- [23] T.J.R. Hughes, J.A. Cottrell, Y. Bazilevs, Isogeometric analysis: CAD, finite elements, NURBS, exact geometry and mesh refinement, *Computer Methods in Applied Mechanics and Engineering* 194 (39–41) (2005) 4135–4195.
- [24] J. Kiendl, R. Schmidt, R. Wüchner, K.-U. Bletzinger. Isogeometric shell analysis with Kirchhoff–Love elements, *Computer Methods in Applied Mechanics and Engineering* 198 (49–52) (2009) 3902–3914.
- [25] G.R. Liu. *Meshfree Methods: Moving Beyond the Finite Element Method*, 2nd ed., CRC Press, Boca Raton, 2009.
- [26] M. Majeed, F. Cirak. Isogeometric analysis using manifold-based smooth basis functions, *Computer Methods in Applied Mechanics and Engineering* 316 (2017) 758–781.
- [27] Q. Zhang, F. Cirak, Manifold-based isogeometric analysis basis functions with prescribed sharp features, *Computer Methods in Applied Mechanics and Engineering* 359 (2020) 112659.
- [28] J.-S. Chen, M. Hillman, S.-W. Chi, Meshfree methods: Progress made after 20 years, *Computational Mechanics* 59 (6) (2017) 733–755. DOI: 10.1007/s00466-017-1414-1.
- [29] T. Belytschko, Y.Y. Lu, L. Gu, Element-free Galerkin methods, *International Journal for Numerical Methods in Engineering* 37(2) (1994) 229–256.
- [30] W.K. Liu, S. Jun, Y.F. Zhang, Reproducing kernel particle methods, *Computational Mechanics* 20 (1995) 108–116. DOI: 10.1007/BF00350275.

- [31] E.J. Kansa, Multiquadrics—a scattered data approximation scheme with applications to computational fluid-dynamics—I. Surface approximations and partial derivative estimates, *Computers & Mathematics with Applications* 19 (8–9) (1990) 127–145. DOI: 10.1016/0898-1221(90)90109-6.
- [32] E. Larsson, E. Lehto, A. Heryudono, B. Fornberg, Stable computation of differentiation matrices and scattered node stencils based on Gaussian radial basis functions, *SIAM Journal on Scientific Computing* 35 (4) (2013) A2096–A2119.
- [33] B. Fornberg, N. Flyer, Solving PDEs with radial basis functions, *Acta Numerica* 24 (2015) 215–258.
- [34] N. Flyer, G.B. Wright, B. Fornberg, Radial basis function-generated finite differences: A mesh-free method for computational geosciences, in: *Handbook of Geomathematics*, Springer, 2015, pp. 1–30.
- [35] C. Shu, H. Ding, K.S. Yeo, Local radial basis function-based differential quadrature method and its application to solve two-dimensional incompressible Navier-Stokes equations, *Computer Methods in Applied Mechanics and Engineering* 192 (7–8) (2003) 941–954.
- [36] Rong Tian, Albert C. To, WingKam Liu, Conforming local meshfree method, *International Journal for Numerical Methods in Engineering* 86 (2011) 335–357.
- [37] G. H. Shi, Manifold method of material analysis, in: *Transactions of the 9th Army Conference on Applied Mathematics and Computing*, No. 92-1, U.S. Army Research Office, Minneapolis, Minnesota, (1991) 57–76.
- [38] G. H. Shi, Modeling rock joints and blocks by manifold method, in: *Proceedings of the 33rd U.S. Symposium on Rock Mechanics*, American Rock Mechanics Association, USRMS, Santa Fe, New Mexico, 1992, pp. 639–648.
- [39] I. Babuška, J.M. Melenk. The partition of unity method, *International Journal for Numerical Methods in Engineering* 40(4) (1997) 727–758.
- [40] J.M. Melenk, I. Babuška, The partition of unity finite element method: Basic theory and applications, *Computer Methods in Applied Mechanics and Engineering* 139 (1996) 289–314.
- [41] T. Strouboulis, I. Babuška, K. Copps, The design and analysis of the Generalized Finite Element Method, *Computer Methods in Applied Mechanics and Engineering* 181 (2000) 43–69.
- [42] C. A. Duarte, I. Babuška, J. T. Oden, Generalized finite element methods for three-dimensional structural mechanics problems, *Computers & Structures* 77 (2000) 215–232.
- [43] T. Belytschko, T. Black, Elastic crack growth in finite elements with minimal remeshing, *International Journal for Numerical Methods in Engineering* 45 (1999) 601–620.
- [44] N. Moës, J. Dolbow, T. Belytschko, A finite element method for crack growth without remeshing, *International Journal for Numerical Methods in Engineering* 46(1) (1999) 131–150.
- [45] T. Strouboulis, K. Copps, I. Babuška, The generalized finite element method, *Computer Methods in Applied Mechanics and Engineering* 190 (2001) 4081–4193.
- [46] Rong Tian, Genki Yagawa, Haruo Terasaka, Linear dependence problems of partition of unity-based generalized FEMs, *Computer Methods in Applied Mechanics and Engineering* 195 (37–40) (2006) 4768–4782.

- [47] Rong Tian, A PU-based 4-node quadratic tetrahedron and linear dependence elimination in three dimensions, *International Journal of Computational Methods* 3 (2006) 545–562.
- [48] Rong Tian, Genki Yagawa, Generalized node and high-performance elements, *International Journal for Numerical Methods in Engineering* 64 (2005) 2039–2071.
- [49] Rong Tian, Hiroshi Matsubara, Genki Yagawa, Advanced 4-node tetrahedrons, *International Journal for Numerical Methods in Engineering* 68 (2006) 1209–1231.
- [50] Rong Tian, Extra-DOF-free and linearly independent enrichments in GFEM, *Computer Methods in Applied Mechanics and Engineering* 266 (2013) 1–22.
- [51] Carsten Riker, Stefan M. Holzer, The mixed-cell-complex partition-of-unity method, *Computer Methods in Applied Mechanics and Engineering* 198 (13–14) (2009) 1235–1248.
- [52] X.M. An, L.X. Li, G.W. Ma, H.H. Zhang, Prediction of rank deficiency in partition of unity-based methods with plane triangular or quadrilateral meshes, *Computer Methods in Applied Mechanics and Engineering* 200 (2011) 665–674.
- [53] X.M. An, Z.Y. Zhao, H.H. Zhang, L.X. Li, Investigation of linear dependence problem of three-dimensional partition of unity-based finite element methods, *Computer Methods in Applied Mechanics and Engineering* 233–236 (2012) 137–151.
- [54] I. Babuška, U. Banerjee, Stable Generalized Finite Element Method (SGFEM), *Computer Methods in Applied Mechanics and Engineering* 201–204 (2012) 91–111.
- [55] A. Sillem, A. Simone, L.J. Sluys, The Orthonormalized Generalized Finite Element Method—OGFEM: Efficient and stable reduction of approximation errors through multiple orthonormalized enriched basis functions, *Computer Methods in Applied Mechanics and Engineering* 287 (2015) 112–149.
- [56] Qinghui Zhang, Ivo Babuška, Uday Banerjee, Robustness in stable generalized finite element methods (SGFEM) applied to Poisson problems with crack singularities, *Computer Methods in Applied Mechanics and Engineering* 311 (2016) 476–502.
- [57] Qinghui Zhang, Ivo Babuška, A stable generalized finite element method (SGFEM) of degree two for interface problems, *Computer Methods in Applied Mechanics and Engineering* 363 (2020) 112889.
- [58] C. Lancaster, K. Salkauskas, Surfaces generated by moving least squares methods, *Mathematics of Computation* 37 (155) (1981) 141–158.
- [59] D. Levin, The approximation power of moving least-squares, *Mathematics of Computation* 67 (224) (1998) 1517–1531.
- [60] H. Wendland, *Scattered Data Approximation*, Cambridge University Press, Cambridge, 2004.
- [61] Rong Tian, LongFei Wen, Improved XFEM — An extra-DOF-free, well-conditioned, and interpolating XFEM, *Computer Methods in Applied Mechanics and Engineering* 285 (2015) 639–658.
- [62] LongFei Wen, Rong Tian, Improved XFEM: Accurate and robust dynamic crack growth simulation, *Computer Methods in Applied Mechanics and Engineering* 308 (2016) 256–285.
- [63] Rong Tian, LongFei Wen, LiXiang Wang, Three-dimensional improved XFEM (IXFEM) for static crack problems, *Computer Methods in Applied Mechanics and Engineering* 343 (2019) 339–367.

- [64] Guizhong Xiao, LongFei Wen, Rong Tian, Arbitrary 3D crack propagation with Improved XFEM: Accurate and efficient crack geometries, *Computer Methods in Applied Mechanics and Engineering* 377 (2021) 113659. DOI: 10.1016/j.cma.2020.113659.
- [65] Guizhong Xiao, LongFei Wen, Rong Tian, Dingguo Zhang, Improved XFEM (IXFEM): 3D dynamic crack propagation under impact loading, *Computer Methods in Applied Mechanics and Engineering* 405 (2023) 115844. DOI: 10.1016/j.cma.2022.115844.
- [66] JinWei Ma, QingLin Duan, Rong Tian, A generalized finite element method without extra degrees of freedom for large deformation analysis of three-dimensional elastic and elastoplastic solids, *Computer Methods in Applied Mechanics and Engineering* 392 (2022) 114639.
- [67] LongFei Wen, Rong Tian, LiXiang Wang, Chun Feng, Improved XFEM for multiple crack analysis: Accurate and efficient implementations for stress intensity factors, *Computer Methods in Applied Mechanics and Engineering* 411 (2023) 116045.
- [68] LiXiang Wang, LongFei Wen, Rong Tian, Chun Feng, Improved XFEM (IXFEM): Arbitrary multiple crack initiation, propagation and interaction analysis, *Computer Methods in Applied Mechanics and Engineering* 421 (2024) 116791.
- [69] P. Hansbo, A. Hansbo, An unfitted finite element method, based on Nitsche's method, for elliptic interface problems, *Computer Methods in Applied Mechanics and Engineering* 191 (2002) 5537–5552.
- [70] N. Perrone, R. Kao, A general finite difference method for arbitrary meshes, *Computers & Structures* 5 (1) (1975) 45–58.
- [71] T. Liszka, J. Orkisz, The finite difference method at arbitrary irregular grids and its application in applied mechanics, *Computers & Structures* 11 (1–2) (1980) 83–95.
- [72] J.J. Benito, F. Ureña, L. Gavete, Influence of several factors in the generalized finite difference method, *Applied Mathematical Modelling* 25 (12) (2001) 1039–1053.
- [73] J. Slak, G. Kosec, Medusa: A C++ Library for Solving PDEs Using Strong Form Mesh-free Methods, *ACM Transactions on Mathematical Software* 47 (3) (2021), Article 28, 25 pages. DOI: 10.1145/3450966.
- [74] G. Tinoco-Guerrero, F.J. Domínguez-Mota, J.A. Guzmán-Torres, G. Pedraza-Jiménez, J.G. Tinoco-Ruiz, mGFD: A meshless generalized finite difference method, *Computers & Mathematics with Applications* 195 (2025) 396–418.
- [75] B. Fornberg, E. Lehto, C. Powell, Stable calculation of Gaussian-based RBF-FD stencils, *Computers & Mathematics with Applications* 65 (4) (2013) 627–637.
- [76] N. Flyer, B. Fornberg, V. Bayona, G.A. Barnett, On the role of polynomials in RBF-FD approximations: I. Interpolation and accuracy, *Journal of Computational Physics* 321 (2016) 21–38.
- [77] V. Bayona, N. Flyer, B. Fornberg, G.A. Barnett, On the role of polynomials in RBF-FD approximations: II. Numerical solution of elliptic PDEs, *Journal of Computational Physics* 332 (2017) 257–273.
- [78] H.W. Kuhn, A.W. Tucker, *Nonlinear Programming*, in: *Proceedings of the 2nd Berkeley Symposium on Mathematical Statistics and Probability*, University of California Press, Berkeley, 1951, pp. 481–492.

- [79] J. Nocedal, S.J. Wright, Numerical Optimization, 2nd ed., Springer, New York, 2006.
- [80] S.H. Christiansen, J. Hu, K. Hu, Nodal finite element de Rham complexes, *Numerische Mathematik* 139 (2) (2018) 411–446.
- [81] L. Beirão da Veiga, F. Brezzi, A. Cangiani, G. Manzini, L.D. Marini, A. Russo, Basic principles of Virtual Element Methods, *Mathematical Models and Methods in Applied Sciences* 23 (1) (2013) 199–214.
- [82] L. Beirão da Veiga, F. Brezzi, L.D. Marini, A. Russo, Virtual Element Methods for general second-order elliptic problems on polygonal meshes, *Mathematical Models and Methods in Applied Sciences* 26 (4) (2016) 729–750.
- [83] D.A. Di Pietro, A. Ern, A hybrid high-order locking-free method for linear elasticity on general meshes, *Computer Methods in Applied Mechanics and Engineering* 283 (2015) 1–21.